A selection of results is presented in Fig. 3 for tensile deformation at 300 K, with emphasis on copper crystals. Although the model does not incorporate ad hoc switches, the resolved stress/strain curves (Fig. 3A) exhibit the traditional stages that characterize fcc single crystals (*16*). The low-hardening stage I, during which a single slip system is activated, appears for low-symmetry orientations like [123]. The linear stage II is due to forest hardening, and its slope increases with the number of active slip systems. The subsequent decrease in strain hardening rate is also orientation-dependent and stems from dynamic recovery. All of these features are in excellent agreement with published experimental results (*16*, *17*). Figure 3B shows the evolution of the shear strains and densities on the primary and secondary slip systems during a simulated [123] test. It is representative of the wealth of detailed information that can be obtained at the scale of slip systems. Finally, Fig. 3C illustrates a broader aspect of this type of modeling by presenting [123] stress/strain curves for several fcc crystals at room temperature. In addition to a rescaling of lattice parameters and elastic constants, shifting from one fcc material to the other implies changes in the annihilation properties of screw dislocations during dynamic recovery. To address this, we tentatively used a scaling law derived from Escaig's model for cross-slip (*4*).

The present results indicate that, paradoxically, realistic strain hardening properties in uniaxial deformation are obtained without accounting for dislocation patterning (*18*, *19*); that is, for the emergence of non-uniform microstructures during plastic flow. A possible reason is that the wavelength of dislocation patterns and the mean free path values follow the same scaling relation, in tension or compression.

This study shows that the mean free path of dislocations is the missing link connecting discrete dislocation interactions and avalanche processes to strain hardening properties in the bulk. The present multiscale methodology should apply to several areas of practical importance, such as the mechanical response of polycrystalline materials or size effects in small dimensions.

References and Notes

1. J. Friedel, *Dislocations* (Pergamon, Oxford, 1967).
2. J. Hirth, J. Lothe, *Theory of Dislocations* (Krieger, Malabar, FL, 1992).
3. A. H. Cottrell, in *Dislocations in Solids*, vol. 11, F. R. N. Nabarro, M. S. Duesbery, Eds. (Elsevier, Amsterdam, 2002), p. vii.
4. Simulation methods and additional information are available as supporting material on *Science* Online.
5. B. Devincre, L. Kubin, T. Hoc, *Scr. Mater.* **54**, 741 (2006).
6. V. V. Bulatov *et al.*, *Nature* **440**, 1174 (2006).
7. V. Bulatov, F. Abraham, L. Kubin, B. Devincre, S. Yip, *Nature* **391**, 669 (1998).
8. R. Madec, B. Devincre, L. Kubin, T. Hoc, D. Rodney, *Science* **301**, 1879 (2003).
9. P. Franciosi, M. Berveiller, A. Zaoui, *Acta Metall.* **28**, 273 (1980).
10. U. F. Kocks, H. Mecking, *Prog. Mater. Sci.* **48**, 171 (2003).
11. C. Teodosiu, J.-L. Raphanel, L. Tabourot, in *Large Plastic Deformations*, C. Teodosiu, J. L. Raphanel, F. Sidoroff, Eds. (A. A. Balkema, Rotterdam, Netherlands, 1993), p. 153.
12. M.-Carmen Miguel, A. Vespignani, S. Zapperi, J. Weiss, J.-R. Grasso, *Nature* **410**, 667 (2001).
13. F. F. Csikor, C. Motz, D. Weygand, M. Zaiser, S. Zapperi, *Science* **318**, 251 (2007).
14. B. Devincre, L. Kubin, T. Hoc, *Scr. Mater.* **57**, 905 (2007).
15. T. Hoc, C. Rey, J.-L. Raphanel, *Acta Mater.* **49**, 1835 (2001).
16. T. E. Mitchell, *Prog. Appl. Mater. Res.* **6**, 117 (1964).
17. T. Takeuchi, *Trans. JIM* **16**, 629 (1975).
18. L. Kubin, *Science* **312**, 864 (2006).
19. L. Kubin, B. Devincre, T. Hoc, *Mater. Sci. Eng. A* **483–484**, 19 (2008).

20. The authors acknowledge funding by their host institutions: CNRS, ONERA, and Ecole Centrale Paris.

Supporting Online Material

www.sciencemag.org/cgi/content/full/320/5884/1745/DC1
SOM Text
Fig. S1
References

5 February 2008; accepted 2 May 2008
10.1126/science.1156101

Ordered Mesoporous Materials from Metal Nanoparticle–Block Copolymer Self-Assembly

Scott C. Warren,[1,2] Lauren C. Messina,[2] Liane S. Slaughter,[2] Marleen Kamperman,[1] Qin Zhou,[2] Sol M. Gruner,[3] Francis J. DiSalvo,[2] Ulrich Wiesner[1]*

The synthesis of ordered mesoporous metal composites and ordered mesoporous metals is a challenge because metals have high surface energies that favor low surface areas. We present results from the self-assembly of block copolymers with ligand-stabilized platinum nanoparticles, leading to lamellar CCM-Pt-4 and inverse hexagonal (CCM-Pt-6) hybrid mesostructures with high nanoparticle loadings. Pyrolysis of the CCM-Pt-6 hybrid produces an ordered mesoporous platinum-carbon nanocomposite with open and large pores (≥10 nanometers). Removal of the carbon leads to ordered porous platinum mesostructures. The platinum-carbon nanocomposite has very high electrical conductivity (400 siemens per centimeter) for an ordered mesoporous material fabricated from block copolymer self-assembly.

Despite considerable progress in the field of porous solids, major challenges remain in the synthesis of ordered mesoporous materials with high metal content from the coassembly of macromolecular surfactants and inorganic species. Controlling the structure of metals at the mesoscale (2 to 50 nm) is crucial for the development of improved fuel cell electrodes and may also assist in the miniaturization of optical and electronic materials for data transmission, storage, and computation (*1*, *2*).

An early route to preparing mesoporous metals involves the dealloying of a less noble metal from a bimetallic alloy; this has been used for the preparation of Raney nickel and other metals (*3*). Dealloying processes provide limited control over structural parameters such as pore geometry and order. In contrast, block copolymer self-assembly or templating with metal species provides access to highly ordered structures. Synthetic routes to such structures have included adsorbing and then reducing metal ions within a preassembled block copolymer scaffold (*4*) and coassembling ligand-stabilized nanoparticles (NPs) with block copolymers (*5*). More recently, polymer-coated NPs that behave like surfactants have been isolated at the interface of block copolymer domains, which can create a bicontinuous morphology at higher loadings (*6*).

Despite this progress, the conversion of metal-polymer hybrids into mesoporous materials with ordered and large pores (≥10 nm) has not been accomplished, in part because of the low volume fraction of metals in most hybrids and the widespread use of gold, which has a high diffusion coefficient and therefore retains its mesostructure only at low temperatures (*7*–*9*). Although a protective organic layer can be added to metal NPs to prevent uncontrolled aggregation, even a thin organic layer represents a considerable volume of the overall material: For example, a 1-nm-diameter metal NP with a relatively thin 1-nm organic shell is just 4% metal by volume. As a result, the typical metal content in most block copolymer–metal NP hybrids is only a few volume %, and the prospects for converting the hybrid into an ordered mesoporous material, in which the metal would have a volume fraction between 60 and 75% for an inverse hexagonal structure, are poor.

Mesoporous metals have been synthesized at a smaller length scale, with 2- to 4-nm pores, through the coassembly of metal ions with small-molecule surfactants followed by reduction (*10*–*13*). The small pore size, however, limits the flow of liquids through the material, which is essential for many applications (*14*, *15*). Metals have also been deposited onto (*16*) or into (*17*) thin films of block

[1]Department of Materials Science and Engineering, Cornell University, Ithaca, NY 14853, USA. [2]Department of Chemistry and Chemical Biology, Cornell University, Ithaca, NY 14853, USA. [3]Department of Physics, Cornell University, Ithaca, NY 14853, USA.

*To whom correspondence should be addressed. E-mail: ubw1@cornell.edu

copolymers to create metal wires, but the surface-dependent nature of the metal deposition most likely limits these processes to two-dimensional materials.

We report a route to mesostructured Pt NP–block copolymer hybrids with exceptionally high NP loadings and tunable phase-separated morphologies with feature sizes >10 nm. Metal-rich NPs with a thin organic shell made from ionic liquid ligands, combined with NP loadings as high as 79 volume % in the hydrophilic domains of the hybrid, ensure that mesostructure order is retained upon conversion to mesoporous metal-C composites. The C can be removed from the nanocomposites to produce ordered Pt mesostructures with ordered and large (≥10 nm) uniform pores.

We used a strategy in which ligand-stabilized Pt NPs (Fig. 1, A and B) coassemble with block copolymers (Fig. 1C) during the evaporation of organic solvents, forming metal-rich mesostructured NP–block copolymer hybrids (Fig. 1D). Hybrids are pyrolized by heating under an inert atmosphere, leaving behind ordered mesoporous Pt-C composites (Fig. 1E). Finally, the C is removed through use of an Ar-O plasma or acid etch to produce ordered porous Pt mesostructures (Fig. 1F). The success of this strategy depends on the synthesis of mesostructured hybrids with high metal volume fractions in one domain of the block copolymer, which is possible after meeting the following criteria.

First, the NPs should exhibit high solubility in organic solvents. When NPs have low solubility, some fraction of the particles macroscopically precipitates during solvent evaporation and fails to mix with the block copolymer. We recently reported a ligand for metal NPs based on a thiol-containing ionic liquid (*18*) that imparted liquidlike behavior to the NPs, even in the absence of a solvent. This result suggests that the use of certain ionic liquids as NP ligands provides a route to high solubility.

Second, the ligand-stabilized NPs should have at least a modest metal volume fraction. Although metal NPs with high solubility have been reported (*18*, *19*), the metal volume fraction was between 0.6 and 3% (*18*). Higher metal volume fractions are needed to prevent structural collapse upon removal of the organic components. Conventional short ligands can increase the metal volume fraction but usually result in insufficient solubility.

Third, the NPs should be highly dispersible in just one block of the block copolymer (*2*, *20*). Mixing should be driven by favorable enthalpic interactions between that block and the NPs, which can be achieved through ionic interactions, hydrogen bonding, and dipole-dipole interactions, among many possible routes.

Fourth, in order to promote mixing, the diameter of the NPs should be below a critical limit relative to the size of the block with which they mix, approximately the root mean square end-to-end distance (equivalent to $6^{1/2}$ times the radius of gyration for an ideal chain) of the relevant block of the copolymer (*21*). Although the precise cutoff may vary depending on enthalpic considerations and NP concentration, this heuristic provides a guideline for NP size.

We designed ligand-stabilized Pt NPs (Fig. 1, A and B) and a block copolymer (Fig. 1C) that met these four criteria. Two poly(isoprene-*block*-dimethylaminoethyl methacrylate), PI-*b*-PDMAEMA block copolymers (a and b) were synthesized by anionic polymerization (*22*) and had a polydispersity of 1.05 (a) or 1.04 (b) and molecular weights of 31.1 (a) or 27.8 (b) kg/mol, of which 33 (a) or 15 (b) weight % (wt %) was PDMAEMA. After examining a series of possible ligands for the Pt NPs, we selected *N,N*-di-2-propoxyethyl-*N*-3-mercaptopropyl-*N*-methylammonium chloride (Fig. 1A). The synthesis of this ligand as well as the ligand-stabilized Pt NPs are described in the supporting online material (SOM) (*23*).

Transmission electron microscopy (TEM) revealed that the NPs had a metal core diameter of 1.8 ± 0.5 nm (Fig. 2A), and a model of the ligand suggested a maximum radial extension of 1.4 nm (Fig. 1B). Nuclear magnetic resonance (NMR) confirmed the chemical structure of the ligand on the NPs, and thermogravimetric analysis (TGA) revealed a metal content of 56.9% by weight, or 7.5% by volume (SOM) (*23*). The NPs exhibited hydrophilic properties: They were highly soluble in methanol, modestly soluble in water and acetone, poorly soluble in chloroform, and insoluble in tetrahydrofuran and ether. We selected a solvent combination of chloroform and methanol [9:1 weight/weight (w/w)], in which both the block copolymer and NPs exhibited high solubility. The NPs were nearly insoluble in the absence of methanol, and the polymer precipitated in solutions with >20% methanol.

The as-synthesized NPs were too hydrophilic to form macroscopically homogeneous hybrids with PI-*b*-PDMAEMA when films were cast from a chloroform:methanol 9:1 (w/w) solution. The NPs became less hydrophilic upon aging. In particular, boiling the NPs for 5 hours in water decreased their hydrophilicity to the extent that they became more soluble in solvents of moderate or low polarity, such as tetrahydrofuran and chloroform. After aging, the NPs were centrifuged to remove the organic byproducts of the aging process. The metal content in the aged NPs was typically 65.4% by mass or 10.4% by volume. The Pt particle size remained unchanged at 1.8 nm,

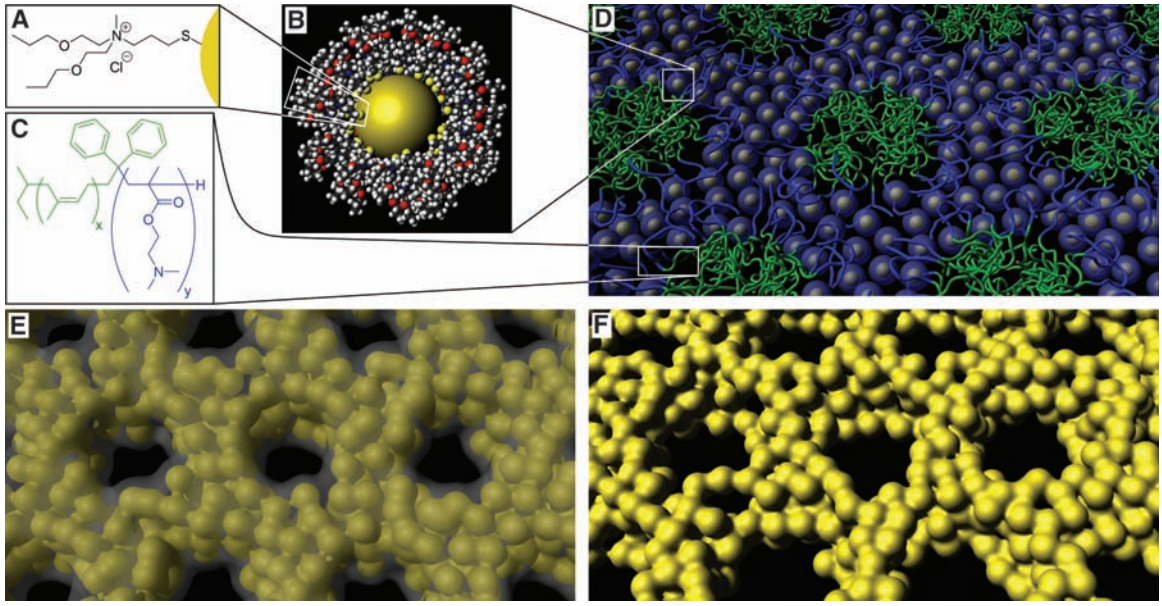

Fig. 1. Illustration of CCM-Pt-6 produced after each stage of the synthesis. (**A**) Chemical structure of *N,N*-di-2-propoxyethyl-*N*-3-mercaptopropyl-*N*-methylammonium chloride, the ligand used to produce moderately hydrophilic Pt NPs with high solubility. (**B**) A true-scale model of a NP with a 1.8-nm-diameter metal core and 1.4-nm ligand shell in which part of the metal surface is artificially exposed for illustrative purposes. The model has the same areal density of ligands as the aged NPs, with about 65 ligands per NP. (**C**) Chemical structure of PI-*b*-PDMAEMA; PI is green and PDMAEMA is blue. [(D) to (F)] Illustrations that attempt to convey the approximate mesostructure geometry and are based on experimental data. (**D**) Self-assembly of Pt NPs with block copolymer followed by annealing affords a hybrid with a regularly ordered structure, such as the inverse hexagonal morphology. (**E**) Pyrolysis of the hybrid under inert atmosphere produces a mesoporous Pt-C composite. (**F**) An Ar-O plasma treatment or acid etch of the Pt-C produces ordered mesoporous Pt.

as measured by TEM, and the Pt domain size increased from 1.2 to 1.4 nm, as determined by peak-width analysis of powder x-ray diffraction (PXRD, Fig. 3B). NMR of the aged NPs showed a spectrum nearly identical to that of the as-synthesized particles (SOM) (*23*). On average, a single aged NP had 65 ligands, a decrease from 93 in the as-synthesized NP (see SOM for calculation) (*23*). The loss of ligands upon heating has been previously documented for planar gold surfaces (*24*) and gold NPs (*25*). Interactions among polymer, ligands, metal surface, and solvents are complex, and the relative contribution of each to NP dispersibility is difficult to determine precisely. We speculate, however, that the substantial decrease in the number of charges per NP (as inferred from the loss of ligands) is responsible for the NPs' diminished hydrophilicity. Furthermore, the loss of ligand may enhance polymer-NP interactions because the PDMAEMA's amine may chemisorb onto the more exposed Pt surface (*26*), thereby preventing the macrophase separation of NPs from block copolymer. Finally, the loss of ligand from the NPs increases the volume fraction of Pt in the NPs by 39%, improving the ability of the mesostructure to survive pyrolysis.

A macroscopically homogeneous solution of aged NPs and block copolymer (a) was prepared by combining 98 mg of NPs, 28 mg of block copolymer, 1040 mg of chloroform, and 110 mg of methanol. The hydrophilic volume fraction [the volume fraction of PDMAEMA and nanoparticles; see SOM for calculations (*23*)] was 65%, which was anticipated to yield a hybrid with an inverse hexagonal mesostructure (CCM-Pt-6). The solution contents were transferred to an aluminum dish 1 cm in diameter and heated at 50°C beneath a hemispherical dish that was designed to slow solvent evaporation. Because chloroform's vapor pressure is greater than that of methanol, and because the solvent composition needed to be maintained near 9:1 chloroform: methanol, a 20-ml vial containing 4 g of chloroform was placed beneath the hemispherical dish, thereby slowing the evaporation of chloroform from the NP–block copolymer solution.

After 1 hour of heating at 50°C, nearly all the solvent had evaporated. The sample was a homogeneous, shiny black solid and was weak and brittle (Fig. 2B). Analysis of the sample by TEM (Fig. 2C) revealed that a mesostructure had formed. The order could be improved, however, by annealing CCM-Pt-6 at 130°C for 2 days under vacuum, as confirmed by small-angle x-ray scattering (SAXS) (Fig. 3A) and TEM (Fig. 2D). Comparison of representative SAXS patterns showed an increased intensity at higher-order reflections for the annealed sample, consistent with a hexagonal lattice (tick marks in Fig. 3A). This structural assignment was corroborated by TEM. The representative TEM image in Fig. 2D revealed an inverse hexagonal mesostructure with grain sizes on the order of a few micrometers. Examination of the mesostructure at higher magnification (Fig. 2E) revealed that individual Pt NPs composed the walls of the CCM-Pt-6 mesostructure, with three to five NPs spanning the thickness of the wall. Comparison of TGA profiles before and after annealing indicated a mass loss of 15% that arose from the loss of ligand (SOM) (*23*). Annealing the sample also caused the diameter of the Pt NPs to increase to 2.3 ± 0.3 nm, as measured by TEM (Fig. 2E). The annealing process thus improves hybrid order and also decomposes the ligands to the extent that the NPs merged and grew. The average grain size of the mesostructure did not increase substantially with longer annealing times, which suggests that ligand decomposition and NP growth were accompanied by a loss in NP mobility.

Besides inverse hexagonal mesostructures (CCM-Pt-6), samples with lamellar morphology (CCM-Pt-4) were produced. We used PI-*b*-PDMAEMA copolymers (a) or (b) to cast hybrids from solution with a hydrophilic volume fraction of 56%. Similarly to the CCM-Pt-6 hybrid, annealing at 130°C led to a well-developed mesostructure as confirmed by SAXS and corroborated by TEM (Figs. 2F and 3A). These results suggest that like oxide structures, metal NP–block co-

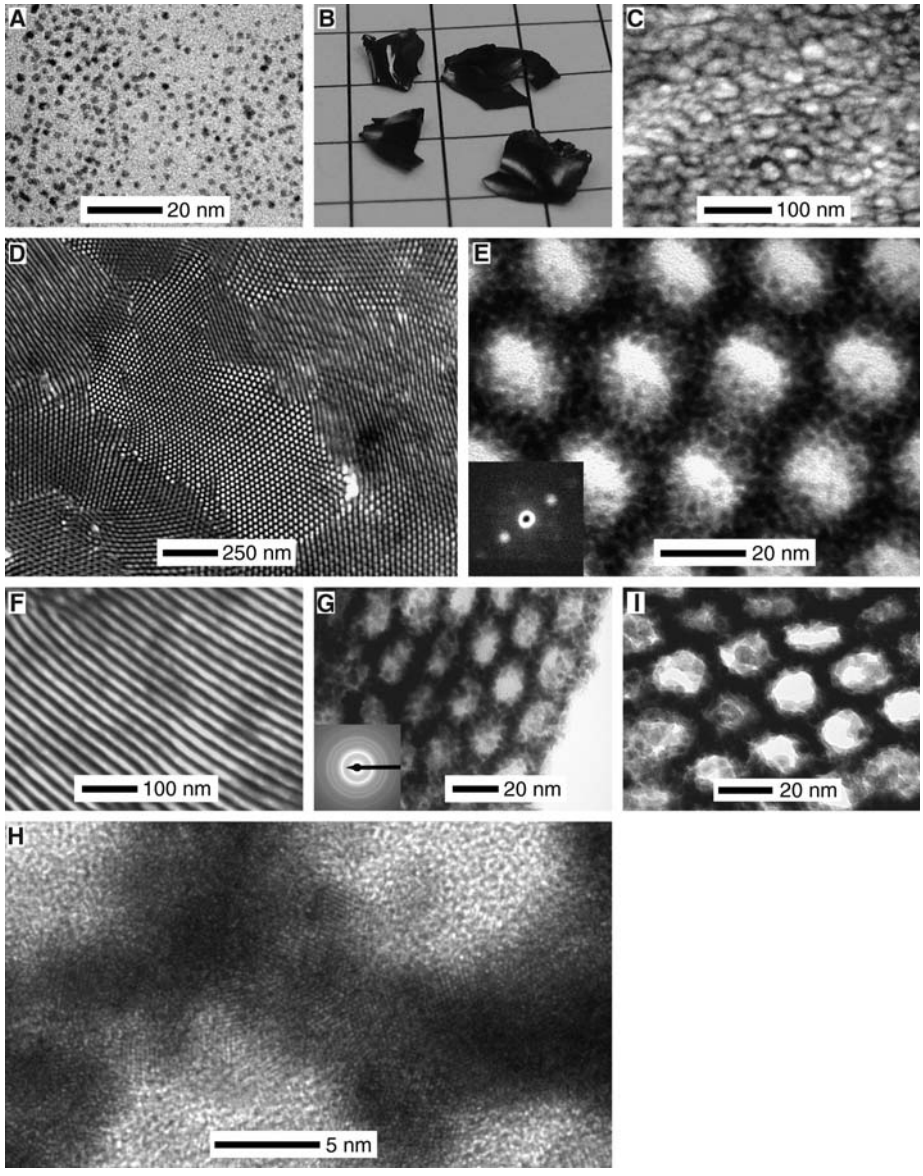

Fig. 2. Bright-field TEM images (A) and (C) to (I) and photograph (B) of materials produced after each stage of the synthesis. (**A**) Ligand-capped Pt NPs. (**B**) Pieces of unannealed CCM-Pt-6 inverse hexagonal hybrid film. The grid paper has 5-mm markings. (**C**) Unannealed inverse hexagonal hybrid. (**D**) An annealed inverse hexagonal hybrid. (**E**) Examination of the hybrid from (D) at higher magnification resolved individual Pt NPs, seen as dark spots in the bright-field image. (Inset) A typical convergent-beam electron diffraction pattern (seen with an ultra–high-vacuum scanning transmission electron microscope) from a single Pt NP, demonstrating its crystallinity. (**F**) An annealed CCM-Pt-4 lamellar hybrid. (**G**) Pyrolysis of an annealed inverse hexagonal hybrid yields a mesoporous Pt-C composite. (Inset) Selected area electron diffraction, showing Pt expected face-centered cubic scattering profile. (**H**) HRTEM of the pyrolized sample resolved the Pt's lattice fringes. (**I**) Removal of carbon with an Ar-O plasma yielded mesoporous inverse hexagonal Pt.

polymer hybrid morphologies can be tailored by simply adjusting the NP volume fraction (*27*).

We used a rapid pyrolysis process (*28*, *29*) to convert the inverse hexagonal hybrid CCM-Pt-6 to an ordered mesoporous Pt-C composite. We heated the sample at 10°C/min under N or Ar to at least 410°C, followed by immediate cooling. Under these conditions, the sp^2-hybridized carbons of the PI block decompose into an amorphous C-rich material with slight graphitic character (Fig. 4A) (*29*). As determined by TGA (SOM) (*23*), the pyrolysis led to a mass loss of 28%. Heating the material to temperatures as high as 550°C did not result in further mass loss. The pyrolysis was accompanied by a decrease in the (1,0) *d*-spacing from 30.0 to 23.7 nm, as revealed by analysis of the SAXS patterns (Fig. 3A). Characterization of the resulting material by TEM (Fig. 2G) indicated that the inverse hexagonal structure was preserved.

At the same time, the Pt interface had roughened, because of the growth of the NPs to 3.3 ± 0.9 nm in diameter. A roughened interface upon pyrolysis is consistent with the loss of higher-order peaks observed in the SAXS profile. Examination of the structure by high-resolution TEM (HRTEM) revealed lattice fringes throughout the Pt walls (Fig. 2H), showing that the walls were composed of crystalline Pt. Analysis by PXRD and application of the Scherrer equation indicated that the Pt nanocrystals' domain size was 4.1 ± 0.4 nm (Fig. 3B), representing a substantial increase from the aged NPs. Together, SAXS, PXRD, and TEM analyses provide a consistent picture of a metal-C composite that is macroscopically homogeneous and uniformly mesostructured.

The C plays an important role in maintaining open, uniform pores of CCM-Pt-6 during pyrolysis (*29*). If the hybrid is heated in air instead of an inert atmosphere, the C is removed (a mass loss of 38% occurs) and the mesostructure is lost. This suggests that the Pt NPs experienced reduced mobility and aggregation within the carbonaceous matrix. In contrast, in the absence of C, the NPs sinter in an uncontrolled fashion. The grainy texture in the TEM images after sintering is indicative of C with a low graphite content (Fig. 2, G and H, for TEM and Fig. 1E for illustration), which is confirmed by Raman spectroscopy (Fig. 4A). Graphitic C has signature D and G bands around 1350 cm^{-1} and 1550 cm^{-1}, respectively (*30*). The weak Raman signature of the C in the hybrid is probably caused by the relatively low temperature (410°C) reached during pyrolysis. Finally, N physisorption indicates that the mesopores are open (Fig. 3C) and that 26% of the sample's volume (micropores and mesopores) is open space, as expected for an inverse hexagonal nanocomposite that has pores lined with C. The Brunauer-Emmett-Teller surface area of CCM-Pt-6 is 18 m^2/g, and the pore diameter is 17 nm.

For many applications, such as fuel cells, it is desirable for the metal surface to be completely exposed. We thus sought a route to remove the C from the CCM-Pt-6 nanocomposite. Heating the pyrolized sample in air to 500°C removed the C but also caused the mesostructure to collapse. Instead, we could remove the C from microtomed thin films (~50 nm thick) of the CCM-Pt-6 nanocomposite using an Ar-O plasma. The mesoporous Pt was structurally similar to the Pt-C nanocomposite, as determined by TEM (Fig. 2I). Close inspection of the pores in TEM images revealed that the grainy texture indicative of the C had disappeared. Furthermore, Raman spectra showed the absence of the D and G bands, suggesting that the C material had been successfully removed (Fig. 4A). Alternatively, for thicker films (10 to 100 μm thick), a sulfuric acid:nitric acid 3:1 (v/v) etch at 70°C (*31*) successfully removed most C. Electrochemical data from acid-etched samples indeed confirmed that the metal surface was exposed, showing current densities nearly identical

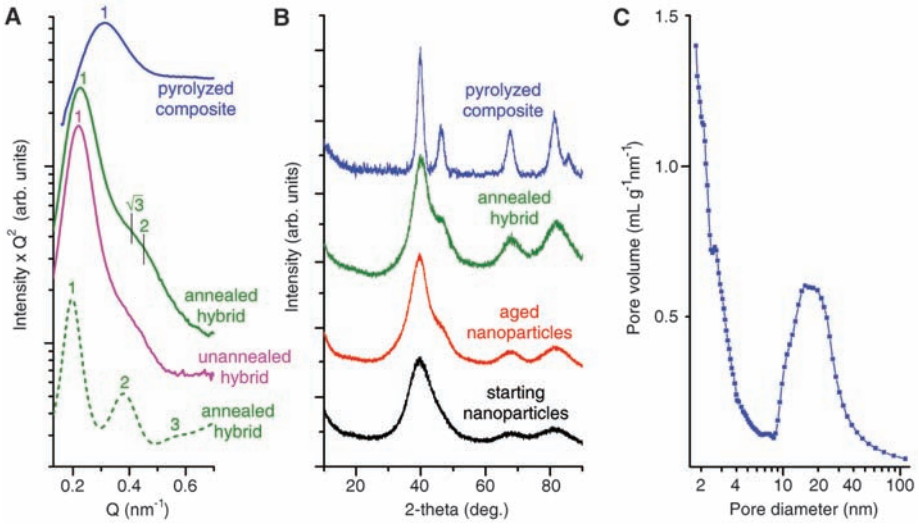

Fig. 3. X-ray and physisorption measurements of materials produced after each stage of the synthesis. (**A**) SAXS profiles of mesostructured materials. *Q*, scattering wavevector. Solid curves correspond to data consistent with an inverse hexagonal mesostructure (CCM-Pt-6), and the dashed curve corresponds to data consistent with a lamellar mesostructure (CCM-Pt-4). For hybrids with the suggested inverse hexagonal hybrid morphology, the (1,0) reflections of the unannealed, annealed, and pyrolized samples correspond to *d*-spacings of 30.3, 30.0, and 23.7 nm, respectively. The first-order reflection of the lamellar sample corresponds to 33.1 nm. Tick marks indicate positions of expected reflections. (**B**) PXRD of samples at various stages of the synthesis. The Pt domain size increases after each stage of processing, from 1.2 nm (starting NPs) to 1.4 nm (aged NPs) to 1.5 nm (annealed hybrid) to 4.1 nm (pyrolized composite), as determined by Scherrer analysis. (**C**) Barrett-Joyner-Halenda pore size distribution as derived from a N physisorption adsorption isotherm reveals a peak mesopore diameter of 17 nm.

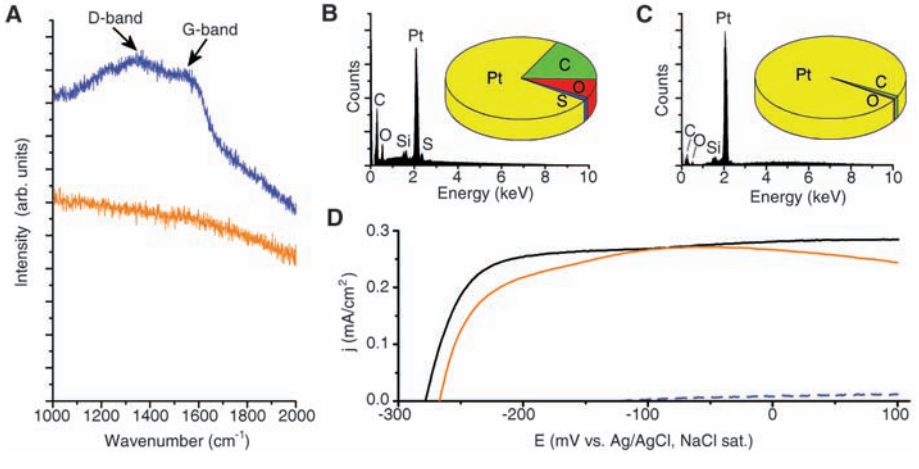

Fig. 4. (**A**) Raman spectra of pyrolized CCM-Pt-6 (top) and Ar-O plasma–treated CCM-Pt-6 (bottom). (**B**) EDS of pyrolized CCM-Pt-6. The pie chart displays elemental weight fractions. The sample was on a Si substrate and the primary energy was 10 keV. Pt = 74 wt %, C = 18 wt %, O = 7 wt %, and S = 1 wt %. (**C**) EDS of acid-treated CCM-Pt-6. Pt = 98 wt %, C = 1 wt %, and O = 0.5 wt %. (**D**) Polarization curves of the H_2 oxidation reaction in H_2-saturated 0.1 M H_2SO_4 solution (at 2000 rpm and 10 mV/s). Blue dashed line, mesoporous Pt-C nanocomposite; orange curve, mesoporous Pt; black curve, planar Pt electrode. *E*, potential; sat., saturated.

to that of bulk Pt (Fig. 4D). Energy-dispersive spectroscopy (EDS) on the CCM-Pt-6 metal-C nanocomposites (Fig. 4B) showed a composition of 74 wt % Pt, 18 wt % C, 7 wt % O, and 1 wt % S. In contrast, after the plasma treatment, EDS revealed that >98 wt % of the sample was Pt, with only trace contributions from C and O (Fig. 4C). C removal was further confirmed by TGA. Pyrolized samples retained 80% of the original mass when heated to 550°C in air, whereas C-etched samples retained 97% of their original mass. TEM confirmed that the samples were still mesostructured and that the grainy texture indicative of C had disappeared.

Because of the easier accessibility of large quantities, we measured the electrical conductivity only of CCM-Pt-6 Pt-C nanocomposites. We chose two-point measurements, which slightly underestimate the true conductivity, because the pyrolized Pt-C composites were too fragile for a four-point measurement, even when pressed as a pellet (*32*). The NP-polymer hybrid had a conductivity of 2.5 mS/cm, which increased to 400 S/cm upon pyrolysis. Despite the presence of C, to the best of our knowledge this value represents the highest electrical conductivity yet measured for ordered mesoporous materials derived from block copolymers.

Because polymer-NP interactions are largely mediated via the nanoparticle ligands, it may be possible to extend the present approach to other metals for which similarly sized ligand-stabilized NPs can be synthesized. Thus, it may be possible to prepare ordered mesoporous metals of other elements, disordered alloys, or even ordered intermetallics. Furthermore, this discovery also creates a potential pathway to a new class of ordered mesoporous metals made from nanoparticles of distinct compositions. Such nanoheterogeneous mesoporous metals may have a range of exceptional electrical, optical, and catalytic properties.

References and Notes

1. A. Haryono, W. H. Binder, *Small* **2**, 600 (2006).
2. A. C. Balazs, T. Emrick, T. P. Russell, *Science* **314**, 1107 (2006).
3. M. Raney, U.S. Patent 1,628,190 (1927).
4. Y. N. C. Chan, R. R. Schrock, R. E. Cohen, *Chem. Mater.* **4**, 24 (1992).
5. D. E. Fogg, L. H. Radzilowski, R. Blanski, R. R. Schrock, E. L. Thomas, *Macromolecules* **30**, 417 (1997).
6. B. J. Kim, G. H. Fredrickson, C. J. Hawker, E. J. Kramer, *Langmuir* **23**, 7804 (2007).
7. P. Buffat, J.-P. Borel, *Phys. Rev. A* **13**, 2287 (1976).
8. R. Li, K. Sieradzki, *Phys. Rev. Lett.* **68**, 1168 (1992).
9. J. Erlebacher, M. J. Aziz, A. Karma, N. Dimitrov, K. Sieradzki, *Nature* **410**, 450 (2001).
10. G. S. Attard *et al.*, *Science* **278**, 838 (1997).
11. G. S. Attard, C. G. Göltner, J. M. Corker, S. Henke, R. H. Templer, *Angew. Chem. Int. Ed. Engl.* **36**, 1315 (1997).
12. Y. Yamauchi, T. Yokoshima, T. Momma, T. Osaka, K. Kuroda, *J. Mater. Chem.* **14**, 2935 (2004).
13. J. Jiang, A. Kucernak, *Chem. Mater.* **16**, 1362 (2004).
14. D. Y. Zhao *et al.*, *Science* **279**, 548 (1998).
15. M. E. Davis, *Nature* **417**, 813 (2002).
16. W. A. Lopes, H. M. Jaeger, *Nature* **414**, 735 (2001).
17. J. Chai, D. Wang, X. Fan, J. M. Buriak, *Nat. Nanotechnol.* **2**, 500 (2007).
18. S. C. Warren *et al.*, *J. Am. Chem. Soc.* **128**, 12074 (2006).
19. S. Sivaramakrishnan, P.-J. Chia, Y.-C. Yeo, L.-L. Chua, P. K. H. Ho, *Nat. Mater.* **6**, 149 (2007).
20. R. B. Thompson, V. V. Ginzburg, M. W. Matsen, A. C. Balazs, *Science* **292**, 2469 (2001).
21. S. C. Warren, F. J. DiSalvo, U. Wiesner, *Nat. Mater.* **6**, 156 (2007).
22. S. Creutz, P. Teyssie, R. Jerome, *Macromolecules* **30**, 6 (1997).
23. See SOM on *Science* Online.
24. E. Delamarche, B. Michel, H. Kang, C. Gerber, *Langmuir* **10**, 4103 (1994).
25. M. J. Hostetler, A. C. Templeton, R. W. Murray, *Langmuir* **15**, 3782 (1999).
26. B. J. Kim, J. Bang, C. J. Hawker, E. J. Kramer, *Macromolecules* **39**, 4108 (2006).
27. M. Templin *et al.*, *Science* **278**, 1795 (1997).
28. C. Liang, K. Hong, G. A. Guiochon, J. W. Mays, S. Dai, *Angew. Chem. Int. Ed.* **43**, 5785 (2004).
29. J. Lee *et al.*, *Nat. Mater.* **7**, 222 (2008).
30. A. C. Ferrari, J. Robertson, *Phys. Rev. B* **61**, 14095 (2000).
31. J. Liu *et al.*, *Science* **280**, 1253 (1998).

32. For future uses in bulk, the material probably will be protected from impact and other damage. Brittleness will not be an issue in static thin-film geometries that are most relevant for applications.

33. The authors acknowledge support of this research by the U.S. Department of Energy (grant DE-FG02-03ER46072) and NSF through a single investigator award (DMR-0605856) as well as through the Cornell Center for Materials Research with funding from the Materials Research Science and Engineering Center program of NSF (cooperative agreement DMR 0520404). X-ray diffraction at the Cornell High Energy Synchrotron Source (CHESS) is supported by NSF under award DMR-0225180. S.C.W. acknowledges support from the Environmental Protection Agency Science to Achieve Results fellowship program. The authors thank H. Abruña for valuable discussions and M. Thomas, A. Burns, J. Lee, and A. Woll for assistance with single-particle electron diffraction, EDS, Raman spectroscopy, and SAXS experimental setup, respectively. A patent application has been submitted based on the findings in this work.

Supporting Online Material

www.sciencemag.org/cgi/content/full/320/5884/1748/DC1
Materials and Methods
SOM Text
Schemes S1 to S3
Figs. S1 to S13
Tables S1 and S2
References

2 May 2008; accepted 29 May 2008
10.1126/science.1159950

Very-High-Energy Gamma Rays from a Distant Quasar: How Transparent Is the Universe?

The MAGIC Collaboration*

The atmospheric Cherenkov gamma-ray telescope MAGIC, designed for a low-energy threshold, has detected very-high-energy gamma rays from a giant flare of the distant Quasi-Stellar Radio Source (in short: radio quasar) 3C 279, at a distance of more than 5 billion light-years (a redshift of 0.536). No quasar has been observed previously in very-high-energy gamma radiation, and this is also the most distant object detected emitting gamma rays above 50 gigaelectron volts. Because high-energy gamma rays may be stopped by interacting with the diffuse background light in the universe, the observations by MAGIC imply a low amount for such light, consistent with that known from galaxy counts.

Ground-based gamma-ray telescopes are sensitive to the Cherenkov light emitted by the electromagnetic showers that are produced by gamma rays interacting in the atmosphere. These telescopes have discovered, since the first detection (in 1989) of gamma rays in this energy range (from 100 GeV to several TeV), more than 20 blazars, which are thought to be powered by accretion of matter onto supermassive black holes residing in the centers of galaxies, and ejecting relativistic jets at small angles to the line of sight (*1*). Most of these objects are of the BL Lac type, with weak or no optical emission lines. Quasar 3C 279 shows optical emission lines that allow a good redshift determination. Satellite observations with the Energetic Gamma Ray Experiment Telescope (EGRET) aboard the Compton Gamma Ray Observatory (CGRO) had measured gamma rays from 3C 279 (*2*) and other quasars, but only up to energies of a few GeV, the limit of the detector's sensitivity. An upper limit for the flux of very-high-energy (VHE) gamma rays was derived in (*3*).

Using MAGIC, the world's largest single-dish gamma-ray telescope (*4*) on the Canary island of La Palma (2200 m above sea level, 28.4°N, 17.54°W), we detected gamma rays at energies from 80 to >300 GeV, emanating from 3C 279 at a redshift of 0.536, which corresponds to a light-travel time of 5.3 billion years. No object has been seen before in this range of VHE gamma-ray energies at such a distance [the highest redshift previously observed was 0.212 (*5*)], and no quasar has been previously identified in this range of gamma-ray energies.

The detection of 3C 279 is important, because gamma rays at very high energies from distant sources are expected to be strongly attenuated in intergalactic space by the possible interaction with low-energy photons ($\gamma + \gamma \rightarrow e^+ + e^-$). These photons [extragalactic back-

*The complete list of authors and their affiliations appears at the end of this paper.

Supporting Online Material for

Ordered Mesoporous Materials from Metal Nanoparticle–Block Copolymer Self-Assembly

Scott C. Warren, Lauren C. Messina, Liane S. Slaughter, Marleen Kamperman, Qin Zhou, Sol M. Gruner, Francis J. DiSalvo, Ulrich Wiesner*

*To whom correspondence should be addressed. E-mail: ubw1@cornell.edu

Published 27 June 2008, *Science* **320**, 1748 (2008)
DOI: 10.1126/science.1159950

This PDF file includes:

Supporting Online Material

Materials and Methods

Block copolymer synthesis. Isoprene (Aldrich, 99%), cyclohexane (J. T. Baker, 99%), THF (J. T. Baker, 99%) and 1,1-diphenylethylene (97%, Aldrich) were distilled from n-butyl lithium (Sigma-Aldrich, 1.6 M in hexanes) before use. DMAEMA (Aldrich, 98%) was distilled from CaH_2 (Aldrich, 90-95%). Methanolic HCl (Supelco, 3 N) was freeze-pump-thawed three times prior to use. Lithium chloride (Aldrich, 99.99%) was evacuated on a vacuum line overnight prior to usage. Sec-butyl lithium (Aldrich, 1.4 M in cyclohexane) was used as received.

Ligand and nanoparticle synthesis. 2-allyloxyethanol (Aldrich, 98%) was distilled from CaH_2 (Aldrich, 90-95%) under nitrogen and freeze-pump-thawed once prior to use. 1,3-dibromopropane (Sigma-Aldrich, 99%) was distilled from potassium carbonate (Sigma-Aldrich, 98%) before use. Pyridine (Aldrich, anhydrous 99.8%), phosphorus tribromide (Aldrich, 99%), 33 wt.% methylamine in ethanol (Aldrich), sodium carbonate (Sigma-Aldrich, 98%), methanol (J. T. Baker, anhydrous, for reaction to make **3** and the nanoparticle synthesis), methanol (Aldrich, anhydrous, 99.8%, for reaction to make **5**), sodium hydrosulfide hydrate (Aldrich), concentrated HCl (Sigma-Aldrich), sodium hydroxide (Sigma-Aldrich, 97%), chloroform (J. T. Baker, 99%), magnesium sulfate (Sigma-Aldrich, anhydrous, 99%), deuterated chloroform (Aldrich, 99.8 atom% D), deuterated water (Aldrich, 99.8 atom% D), platinum (IV) chloride (Aldrich, 99.9%), sodium borohydride (Sigma-Aldrich, 99%), and ether (J. T. Baker, anhydrous) were used as received.

Hybrid synthesis. Methanol (J. T. Baker, anhydrous), and chloroform (J. T. Baker) were used as received. Fisherbrand aluminum weighing dishes (Fisher, 08-732-100, 1-1/16 fl. oz. capacity) were formed into aluminum dishes with a 1 cm diameter by bending the aluminum dish around a cylindrical object with a 1 cm diameter. The walls of the dish were typically bent at a ~45° with respect to the bottom of the dish.

NMR, EM, x-ray and physics methods. Standard Schlenk line techniques were used for the synthesis of the ligand. NMR spectra were acquired on a Mercury 300 at 300 MHz (^{1}H) and 75 MHz (^{13}C). Films were cast beneath a hemispherical dish made from the bottom half of a 1-L flask. Heating was controlled using a IKA RET control visc IKAMAG digital hotplate. Samples were prepared for TEM by sectioning at 60 nm with a Leica Ultracut UCT at -50 °C. The samples were collected on a water/DMSO eutectic solution and transferred to 300 mesh copper grids (no carbon film was used). Most TEM was performed on a Tecnai T12 at 120 kV and high resolution energy filtered (zero loss) TEM was performed on a Tecnai F20 with a Gatan Tridium Spectrometer at 200 kV. Single particle electron diffraction (convergent beam electron diffraction, CBED) was performed on a VG HB501UX UHV-STEM at 100 keV with a 0.2 nm probe. PXRD was performed on a Scintag XDS 2000, with a scan rate of 0.1°/minute, and the full width at half maximum determined using curve fitting within Jade. Every platinum reflection was used in the Scherrer analysis. Energy dispersive spectroscopy (EDS) was performed on a LEO 1550 FE-SEM at 10 kV. TGA was performed using a TA Instruments Q500 instrument equipped with an autosampler. SAXS experiments were performed on a Rigaku RU-H3R copper rotating anode (λ= 1.54 Å) for CCM-Pt-6 and on the G1 station at the Cornell High Energy Synchrotron Source (CHESS) for CCM-Pt-4.

The Rigaku RU-H3R setup was operated at 40 kV and 50 mA. X-rays were monochromated with a Ni filter and focused using orthogonal Franks mirrors. SAXS patterns were collected with a homebuilt 1 K × 1 K pixel CCD detector. The SAXS data obtained at CHESS were collected with a CCD 2-D detector operating at an x-ray energy of 1.223 Å. Nalgene Oakridge Teflon centrifuge tubes were employed for purifying nanoparticles. Centrifugation was performed using an Eppendorf 5810. Physisorption was performed on a Micromeritics ASAP 2020 using nitrogen as the physisorption gas. Raman spectroscopy was performed on a confocal Raman microscope using a Nd:YAG laser at 532 nm.

Statistics about the nanoparticle core diameters were taken from measurement of over 100 particles using intensity profiles drawn in Gatan DigitalMicrograph. The nanoparticle platinum (core) diameter was 1.83 ± 0.5 nm for both as-synthesized and aged particles.

Electrochemistry methods. We first added one small flake of the mesoporous platinum-carbon nanocomposite or mesoporous platinum onto a glassy carbon electrode. Next we added 5 μL of a Nafion solution (5 wt.% solution in alcohol and water) and the liquids were evaporated at room temperature in air. The real surface area of the catalyst was estimated using a conventional procedure based on the coulometry of H_{upd} (taking 210 μC cm^{-2} for a monolayer). A three-electrode cell equipped with the working electrode, a platinum coil counter electrode, and a sodium chloride saturated Ag/AgCl reference electrode was used for all electrochemical measurements.

Block copolymer synthesis

Scheme S1 outlines crucial steps of the polymer synthesis. The synthesis of poly(isoprene-*block*-dimethylaminoethyl methacrylate) (PI-*b*-PDMAEMA) has been previously reported (*1*, *2*). The PI-*b*-PDMAEMA block copolymers were synthesized by anionic polymerization under anhydrous and air-free conditions using a glovebox and Schlenk line techniques.

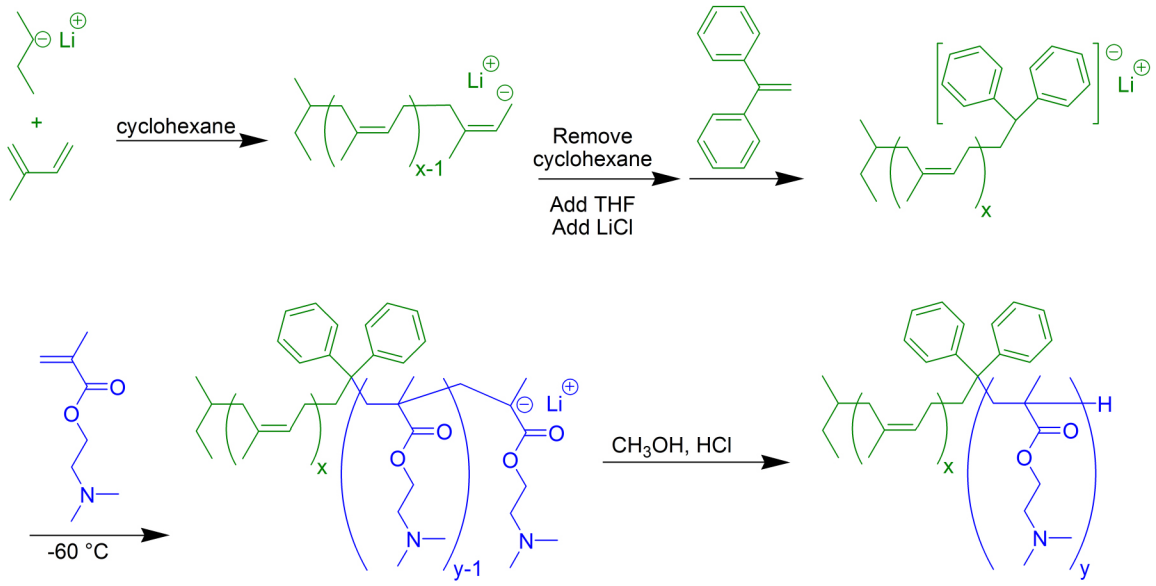

Scheme S1. Synthesis of PI-*b*-PDMAEMA.

Sec-butyl lithium was used to initiate isoprene in cyclohexane. After 8 hours of polymerization, cyclohexane was removed on a vacuum line and anhydrous THF and LiCl were subsequently added to the PI in a glovebox. A small amount of the PI was removed via syringe, terminated with methanolic HCl, and subjected to GPC to determine the PI MW. The polyisoprene was end-capped with a 5-fold excess of diphenylethylene and stirred for 30 min. The polymer solution was cooled to -60 °C before the addition of DMAEMA. The polymerization was allowed to proceed for

several hours before the reaction was terminated with methanolic HCl. To purify the polymer, it was precipitated in cold methanol and dried on a vacuum line for several days. The polymers were characterized by GPC to give the final polydispersity and NMR was used to determine PDMAEMA weight fraction. The polymer (a) used to make a lamellar and inverse hexagonal mesostructure had a polydispersity of 1.05 and a molecular weight of 31.1 kg/mol of which 33 wt.% PDMAEMA. A second polymer (b) used to make a lamellar mesostructure had a polydispersity of 1.04 and a molecular weight of 27.8 kg/mol of which 15 wt.% was PDMAEMA.

Ligand synthesis

The ligand synthesis is depicted in Scheme S2.

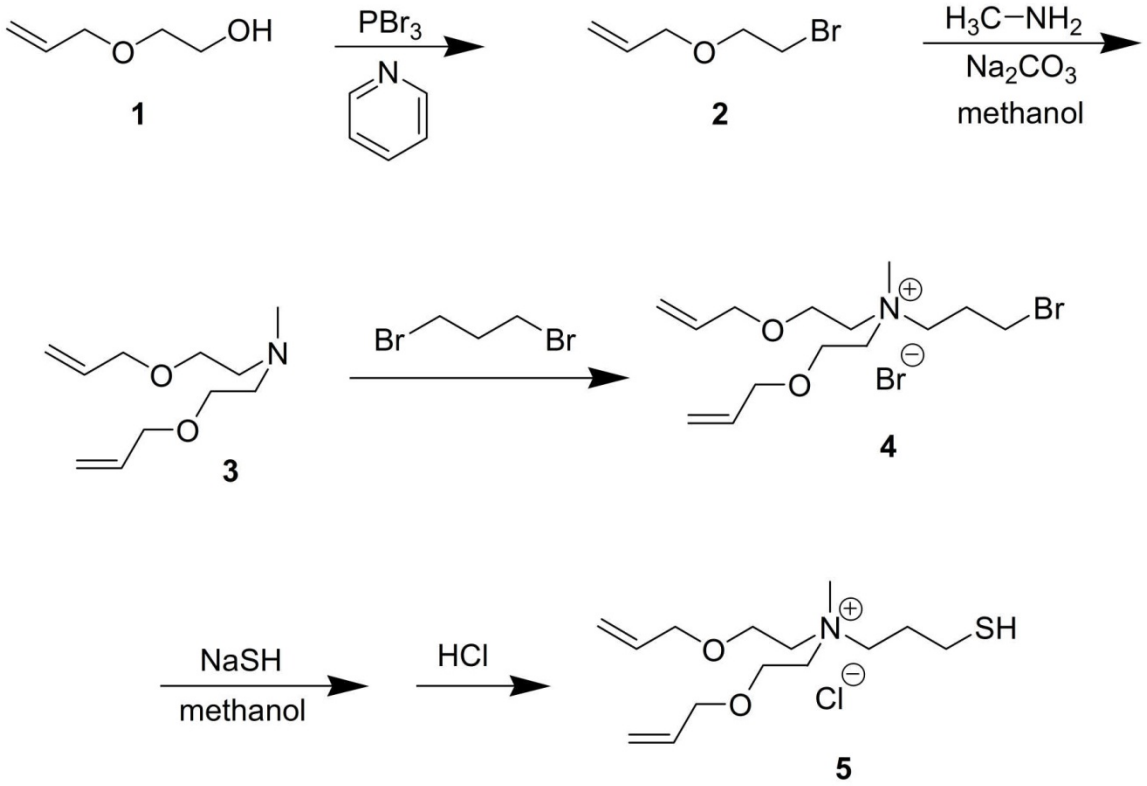

Scheme S2. Synthesis of *N*,*N*-di-2-allyloxyethyl-*N*-3-mercaptopropyl-*N*-methylammonium chloride, **5**.

Allyloxyethylbromide (2). *Warning: 2-allyloxyethanol and its derivatives may possibly be absorbed through skin, especially as vapor and may possibly exhibit toxicity (see Int. Arch. Occup. Environ. Health, **70**, 232-236 (1997)). Care should be taken to handle these compounds in a fume hood.* In a glovebox, 200 g of PBr_3 (0.739 mol) was added to a 1 L round bottom flask containing a large stirbar. Separately, 54 g of anhydrous pyridine (0.683 mol) and 209 g of anhydrous 2-allyloxyethanol, **1**, (2.05 mol) were mixed in a beaker and transferred to a large pressure-equalizing addition funnel. The flask with PBr_3 and the addition funnel were removed from the glovebox, quickly assembled, and maintained beneath an atmosphere of nitrogen. The flask with PBr_3 was cooled in an ice bath with salt to -10 °C. The contents of the addition funnel were delivered to the PBr_3 over the course of 4 hours. Part way through the addition, a white precipitate accumulated in the flask, making stirring difficult. From this point on, the flask was manually swirled every 10 minutes or so to maintain good mixing. After the addition, the reaction was allowed to come to room temperature overnight. The product was distilled out of this mixture under dynamic vacuum, at approximately 0.05 mbar and between 25 and 28 °C. The distillate typically consisted of a mixture of **1** and **2**. A second distillation was used to separate the two; the boiling point of **2** is slightly higher than that of **1**. The reaction afforded 89 g of **2** (0.54 mol), a 26% yield. ^{1}H and ^{13}C NMR spectra are shown in Figures S1 and S2.

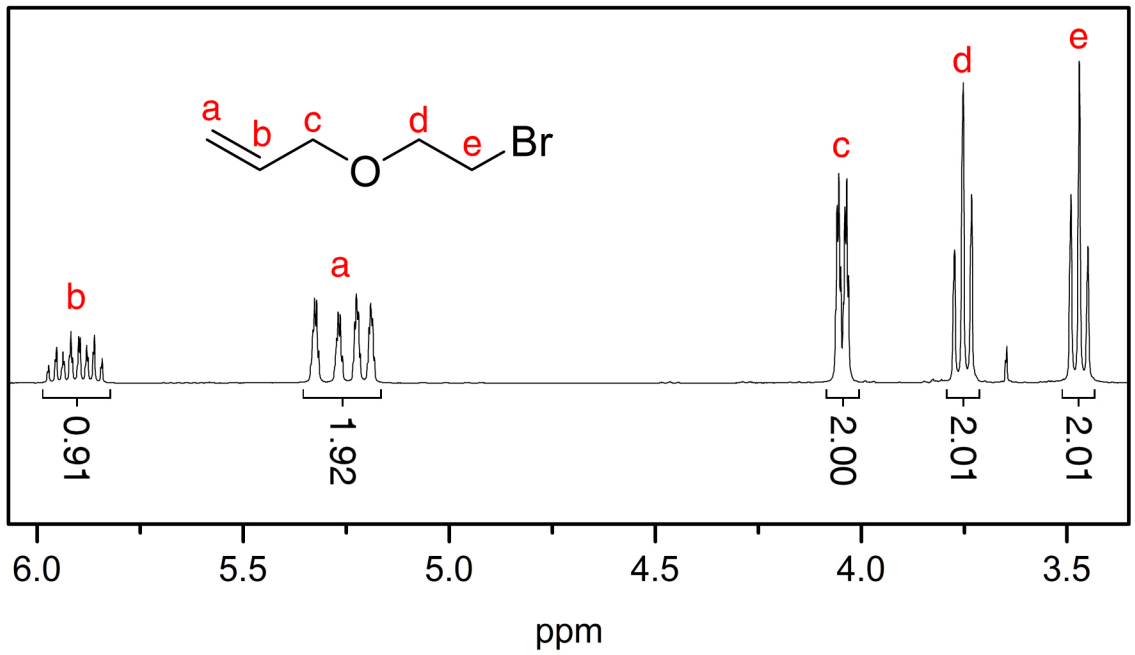

Figure S1. ^{1}H NMR of **2**. ($CDCl_3$, 300 MHz) δ 5.91 (**b**, m, 1H), 5.25 (**a**, m, 2H), 4.04 (**c**, m, 2H), 3.75 (**d**, t, 2H, J = 6.21 Hz), 3.47 (**e**, t, 2H, J = 6.13 Hz).

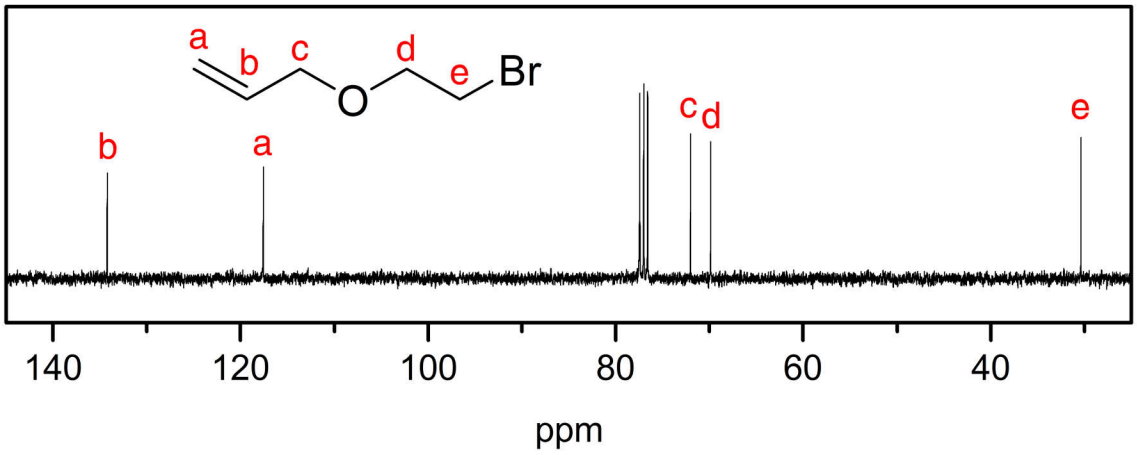

Figure S2. ^{13}C NMR of **2**. ($CDCl_3$, 75 MHz) δ 134.2 (**b**), 117.6 (**a**), 72.0 (**c**), 69.9 (**d**), 30.4 (**e**).

***N,N*-di-(2-(allyloxy)ethyl)-*N*-methylamine (3).** To a 1-L flask with a stirbar, we added 89 g of **2** (0.54 mol), 440 g of methanol, 25.4 g of 33 wt.% methylamine in ethanol

(0.270 mol), and 57.2 g of Na_2CO_3 (0.54 mol). The flask was equipped with a reflux condenser and heated at 36 °C in an oil bath under flowing nitrogen. After one day the temperature was increased to 58 °C. After one day at the elevated temperature the flask was removed from heat. The methanol was removed via rotary evaporation. The slurry was dumped into filter paper and washed with chloroform. The amine was extracted into an aqueous HCl solution from the chloroform solution, followed by extraction into chloroform by lowering the pH to between 12 and 14 with NaOH. The chloroform was dried over $MgSO_4$ for 5 minutes, filtered through Whatman filter paper, and the chloroform was rotary evaporated. The amine was distilled under dynamic vacuum at 51 °C and 0.1 mbar. Often, the amine was fractionally distilled a second time to improve purity. The product was a colorless, transparent liquid. Approximately 8.50 g of **3** (0.0427 mol) was isolated from the reaction, a yield of 8%. The low yield is due to the preferential formation of the *N*,*N*,*N*-tri-(2-(allyloxy)ethyl)-*N*-methylammonium bromide. ^{1}H and ^{13}C NMR spectra are shown in Figures S3 and S4.

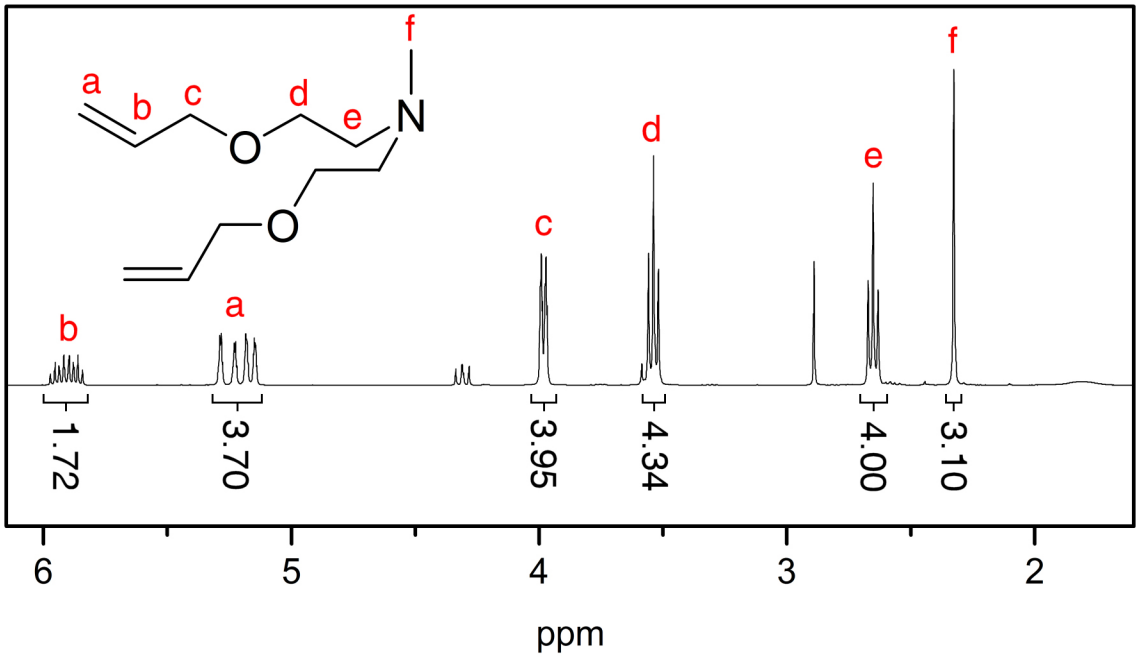

Figure S3. ^{1}H NMR of **3**. ($CDCl_3$, 300 MHz) δ 5.90 (**b**, m, 2H), 5.20 (**a**, m, 4H), 3.98 (**c**, m, 4H), 3.54 (**d**, t, 4H, J = 5.99 Hz), 2.65 (**e**, t, 4H, J = 5.99 Hz), 2.33 (**f**, s, 3H). The unlabeled peaks are from unknown contaminants.

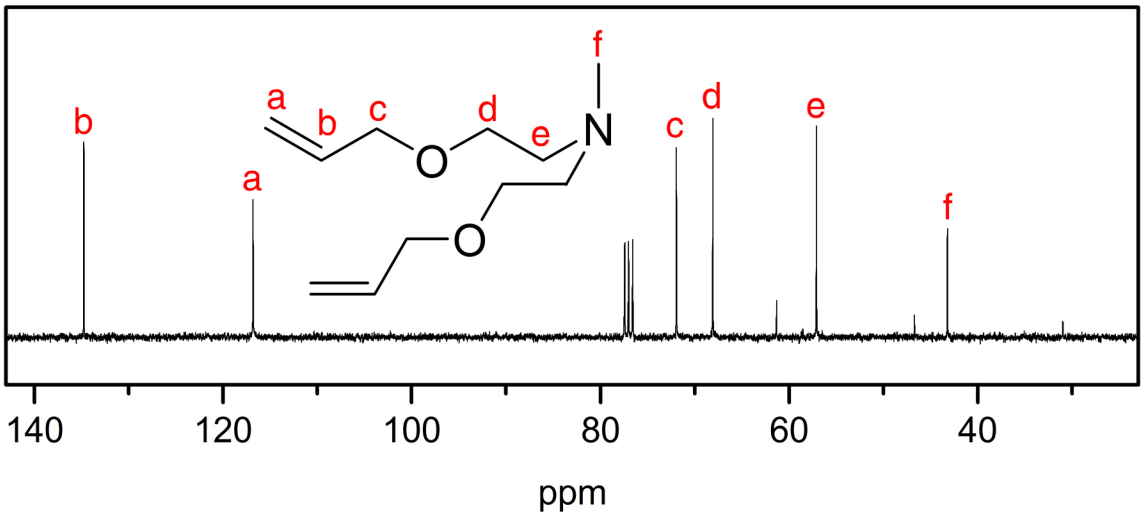

Figure S4. ^{13}C NMR of **3**. ($CDCl_3$, 75 MHz) δ 134.7 (**b**), 116.8 (**a**), 71.9 (**c**), 68.1 (**d**), 57.1 (**e**), 43.2 (**f**).

***N*-3-bromopropyl-*N*,*N*-di-(2-(allyloxy)ethyl)-*N*-methylammonium bromide (4).** We began by weighing a 250 mL flask with stirbar. To this flask we added 8.50 g of **3** (0.0427 mol) and 274.74 g of 1,3-dibromopropane (1.361 mol). The reaction was heated in an oil bath at 50 °C for 16 hours. The excess 1,3-dibromopropane was removed from the reaction via distillation under vacuum. During the distillation, the flask was immersed in an oil bath at 50 °C; heating for prolonged periods at higher temperatures could decompose the product. The 1,3-dibromopropane could be re-used. The flask was connected directly to the vacuum line and evacuated overnight to remove the residual 1,3-dibromopropane. Finally, the flask was brought immediately into a glovebox to prevent the absorption of water. The contents of the flask, **4**, weighed 16.44 g (0.0410 mol), nominally a yield of 96%. The starting material **3** is not entirely pure (see Figures S3, S4), so the actual yield of this reaction is probably close to 100%. ^{1}H and ^{13}C NMR spectra are shown in Figures S5 and S6.

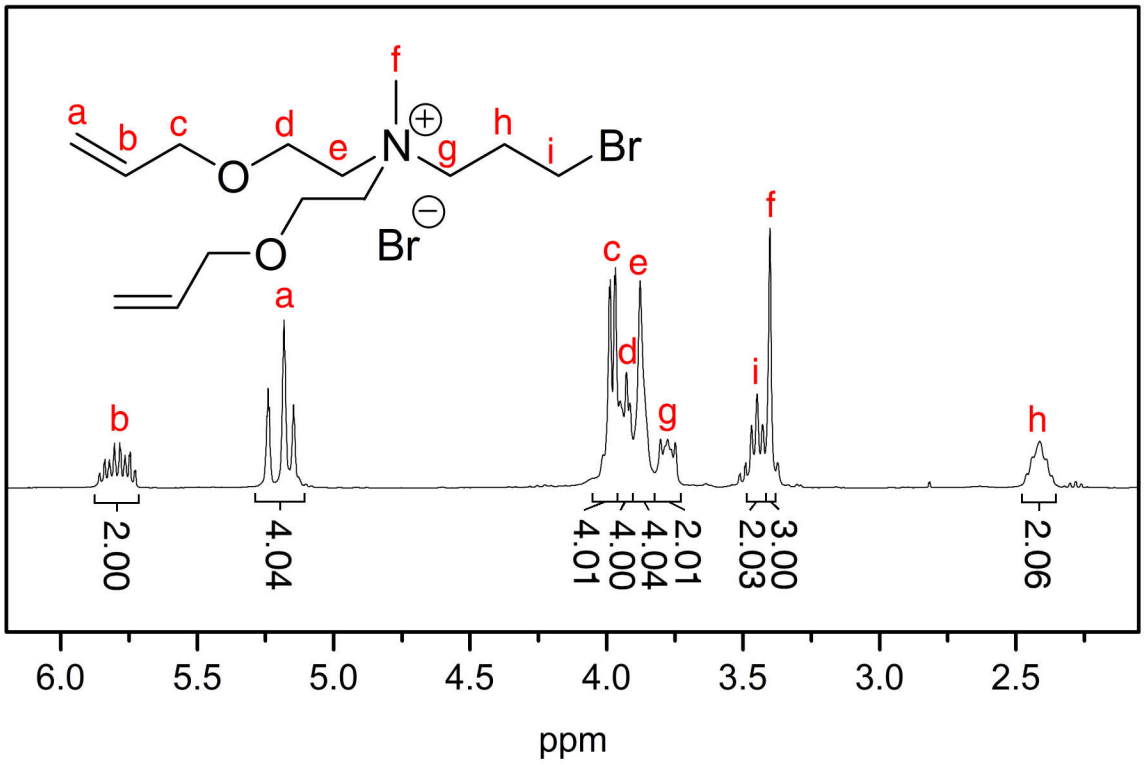

Figure S5. ^{1}H NMR of **4**. ($CDCl_3$, 300 MHz) δ 5.79 (**b**, m, 2H), 5.18 (**a**, m, 4H), 3.98 (**c**, m, 4H), 3.93 (**d**, t, 4H), 3.88 (**e**, t, 4H), 3.78 (**g**, t (restricted rotation), 2H), 3.45 (**i**, t, 2H, J = 5.85 Hz), 3.40 (**f**, s, 3H), 2.41 (**h**, p, 2H, J = 6.91 Hz).

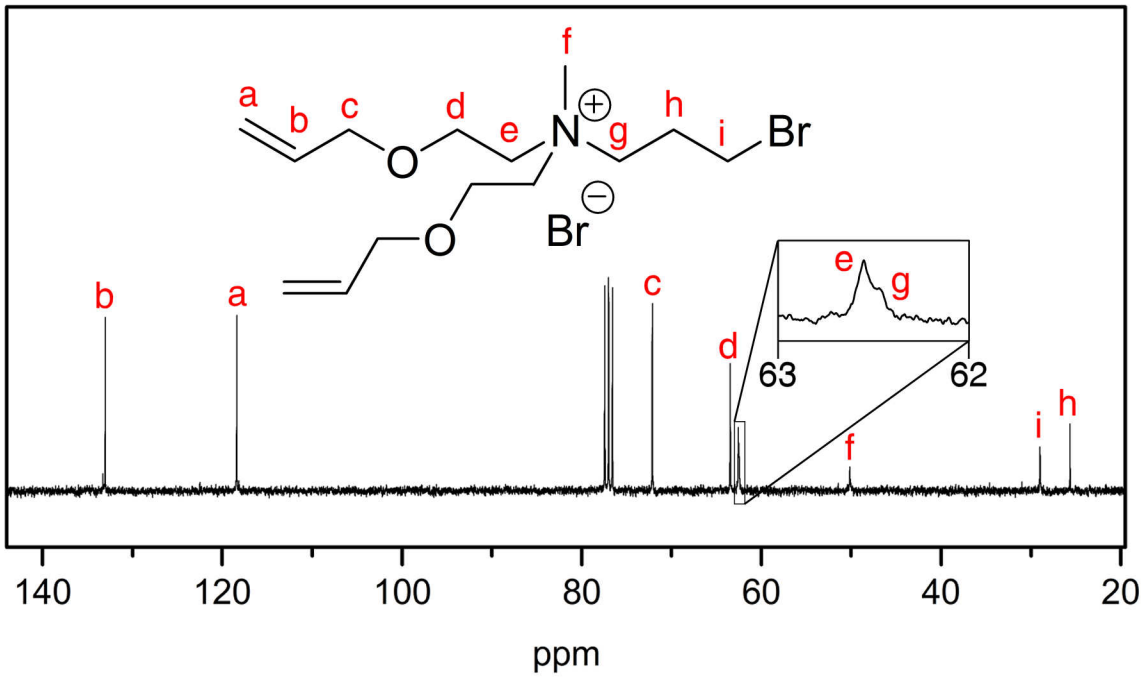

Figure S6. ^{13}C NMR of **4**. ($CDCl_3$, 75 MHz) δ 133.0 (**b**), 118.4 (**a**), 72.5 (**c**), 63.5 (**d**), 62.6 (**e**), 62.5 (**g**), 50.2 (**f**), 29.0 (**i**), 25.6 (**h**).

***N,N*-di-(2-(allyloxy)ethyl)-*N*-3-mercaptopropyl-*N*-methylammonium chloride (5).** To the same flask with 16.44 g of **4** (0.0410 mol) we added 2.490 g of sodium hydrosulfate hydrate in a glovebox (water content varies from bottle to bottle and slowly decreases upon storage in an anhydrous environment; water content is typically less than 35 wt.% and may get as low as a few percent upon lengthy storage). We added 55 g of dry, degassed methanol to solvate the reagents, and assembled the flask with a reflux condenser under flowing nitrogen outside the glovebox. The reaction was heated at 65 °C for 8 hours. The reaction was cooled to room temperature and concentrated HCl was added (in air) until the pH stabilized at <2. Usually at least several mL of concentrated HCl were needed. During the addition NaCl precipitated from solution. The solution was then stirred for at least an hour in a well ventilated fume hood so that any excess

NaSH would react with the HCl and be removed as gaseous H_2S (*Caution! H_2S is a toxic gas which can deaden one's sense of smell and can be fatal at modest concentrations!*) The solution was then rotary evaporated to remove the methanol. The flask with product mixture **5** was attached to a vacuum line for several hours to remove water and HCl. The product mixture was dissolved in chloroform and filtered through Whatman filter paper to remove remaining NaCl or NaBr. The chloroform was rotary evaporated and the product was attached to a vacuum line overnight to remove residual solvent and water. The product mixture **5** is initially a viscous, yellow-orange liquid. Upon sitting for several weeks, the product begins to solidify. As determined by NMR, there is no detectible change upon sitting. The reaction afforded 12.23 g of the product mixture, a yield of 96% assuming exclusive production of **5**. The product was immediately brought into the glovebox to prevent absorption of water. As determined by NMR, the product mixture contains the thiol, disulfide and sulfide of **5** and a small amount of residual **4**. The relative proportions of each vary from synthesis to synthesis and a typical product distribution is shown in Figures S7 and S8. The variation in the product distribution is related to variations in the ratio of **4** and NaSH that are initially combined. An excess of NaSH promotes sulfide formation because NaSH deprotonates thiol **5** to form a thiolate which can nucleophilically substitute for the bromide of **4**. An excess of NaSH probably promotes disulfide formation via deprotonation of the thiol followed by oxidation, possibly by adventitious oxygen. Across five syntheses, thiol content varied between 13% and 45%, sulfide varied between 10 and 18%, disulfide varied between 19 and 43%, and **4** content varied between 20% and 26%. Importantly, variation in the product distribution did not seem to influence the synthesis of the nanoparticles. No further

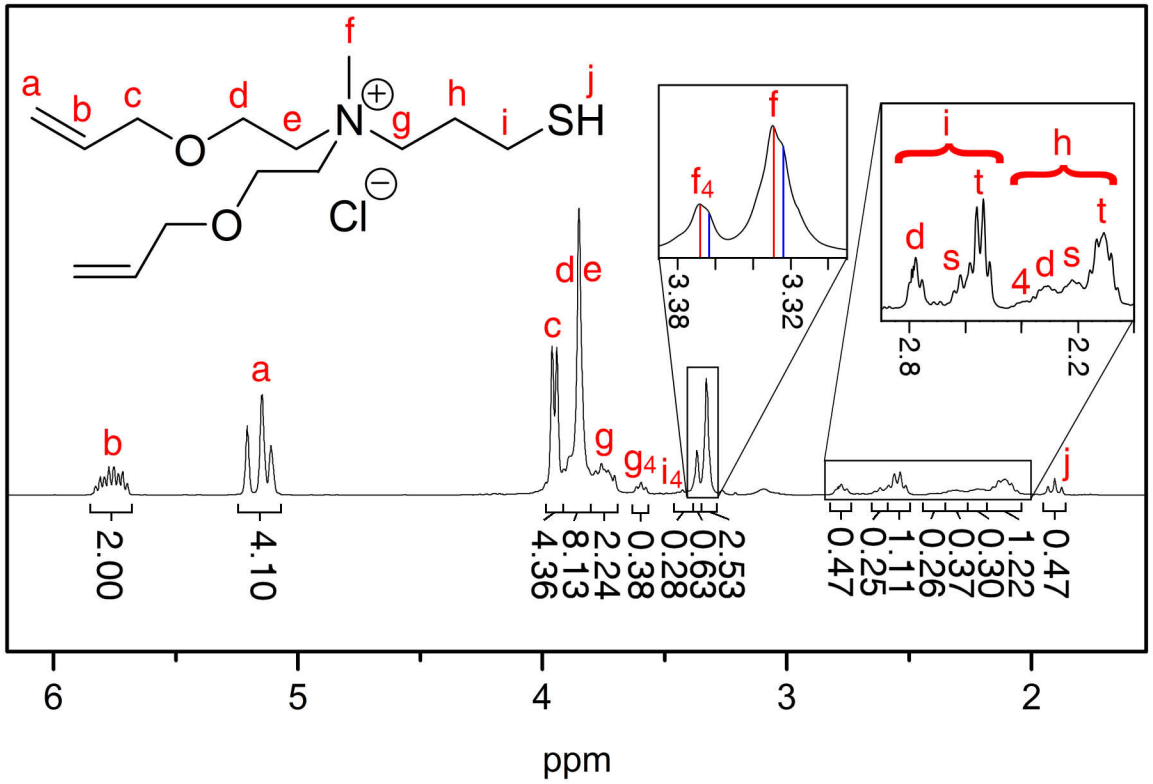

Figure S7. ^{1}H NMR of product mixture **5**. Letters without subscripts (a through j) correspond to **5** as shown in the figure. Letters d, s, and t indicate the disulfide, sulfide, and thiol, respectively, for protons i and h. Letters with a subscript (f_4, g_4, h_4, and i_4) label peaks from residual **4**. Red and blue lines highlight the fact that peaks f an f_4 are the superposition of two smaller peaks. This arises from the presence of both the chloride salt (as drawn in the figure) and the bromide salt (not shown). Red lines correspond to molecules with a chloride anion and blue lines correspond to molecules with a bromide anion. The chloride salt predominates, so this form is what will be drawn throughout this manuscript. ($CDCl_3$, 300 MHz) **Thiol 5**: δ 5.76 (**b**, m, 2H), 5.15 (**a**, m, 4H), 3.95 (**c**, m, 4H), 3.85 (**d**, **e**, t, 8H), 3.75 (**g**, t, 2H), 3.329 (**f**, **chloride**, s, 3H), 3.324 (**f**, **bromide**, s, 3H), 2.55 (**i_t**, q, 2H, J = 7.3 Hz), 2.11 (**h_t**, p, 2H, J = 7.5 Hz), 1.90 (**j**, t, 1H, J = 8.5 Hz).

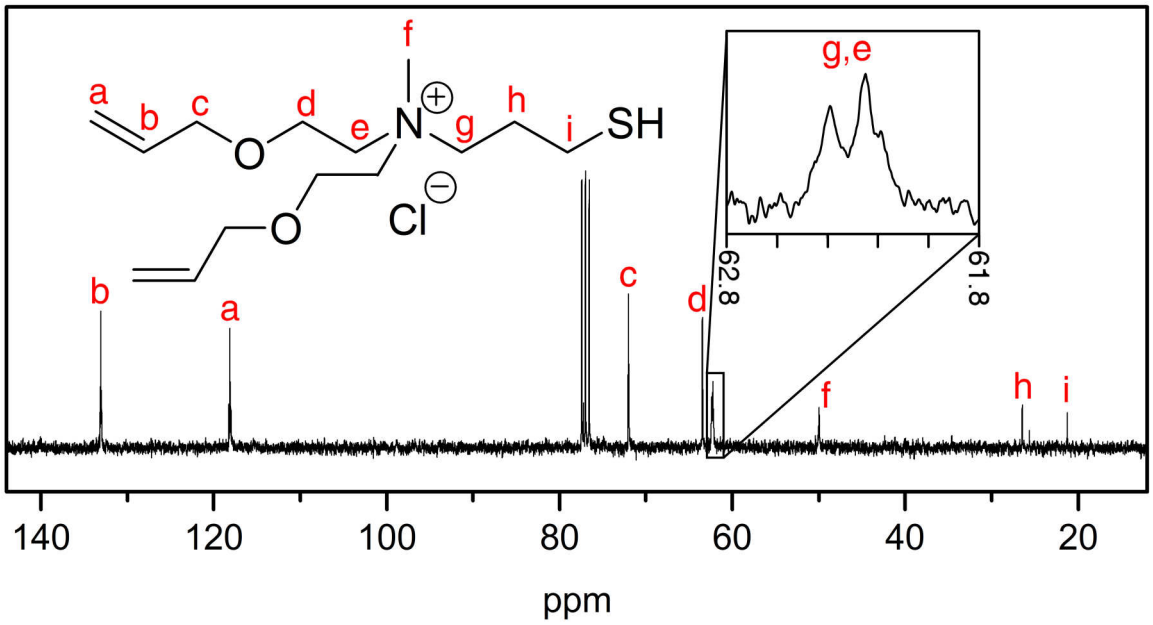

Figure S8. ^{13}C NMR of **5**. ($CDCl_3$, 75 MHz) δ 133.1 (**b**), 118.1 (**a**), 72.0 (**c**), 63.5 (**d**), 62.4, 62.3 (**g**, **e**), 50.0 (**f**), 26.5 (**h**), 21.2 (**i**).

purification was performed. ^{1}H and ^{13}C NMR spectra of a typical product mixture are shown in Figures S7 and S8.

Nanoparticle synthesis

The stages of nanoparticle synthesis, purification, and ageing are depicted in Scheme S3.

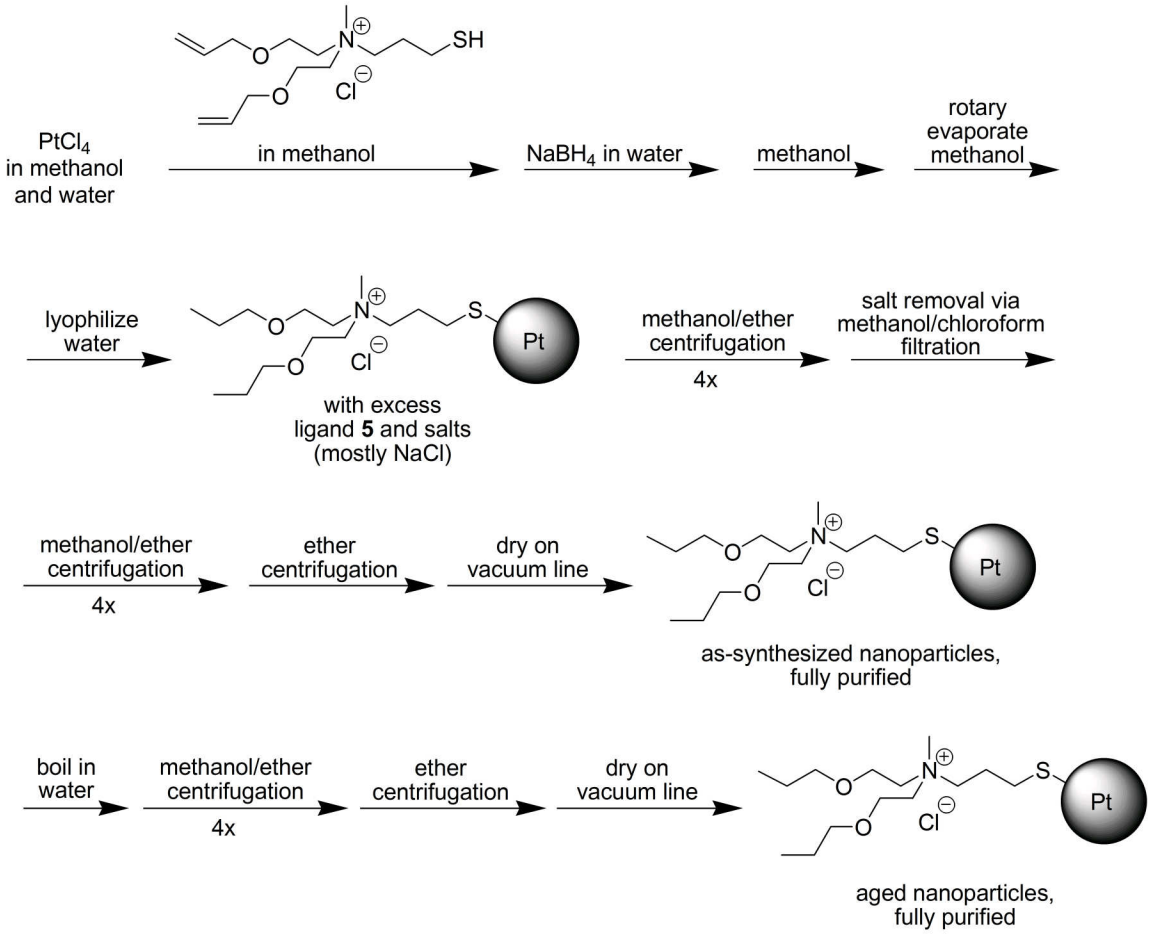

Scheme S3. Nanoparticle synthesis, purification, and ageing.

We performed the nanoparticle synthesis on a variety of scales, using between 1.0 g of $PtCl_4$ and 2.0 g of $PtCl_4$ and scaling the other reagents proportionally. Because of the precise timing required in the synthesis, batches made with more than 2.0 g of $PtCl_4$ were less reproducible, largely because of the challenge in transferring large quantities of reagents in the short times required. Indeed, following the timing described below is essential to obtain Pt nanoparticles with a 1.83 nm diameter and variations from this process tended to give low yields or smaller particles (as small as 1.0 nm).

Three solutions were prepared immediately prior to the nanoparticle synthesis. The first solution was prepared in a one-neck 1-L round bottom flask with a large joint (at least 24/40) and a large stirbar. To this flask we added 2.000 g of $PtCl_4$ (5.937 mmol), 100.0 g of water, and 100.0 g of methanol. The second solution was prepared in a 125 mL Erlenmeyer flask. To this flask we added 1.50 g of **5** and 30.0 g of methanol. The third solution was prepared in a 125 mL Erlenmeyer flask by combining 2.272 g of $NaBH_4$ and 45.0 g of water.

Over a period of about 2 to 3 seconds, the second solution (**5**) was poured into the first solution ($PtCl_4$), while stirring rapidly. About 1 to 2 seconds later, the third solution ($NaBH_4$) was added to the first two solutions over a period of less than 5 seconds. About 10 minutes later, 200 mL of methanol was added to the solution. The solution was stirred for 10 more minutes before the stirbar was removed and the methanol rotary evaporated.

Careful timing in the above steps arises from the tendency of Pt^{4+} to form an insoluble complex with **5** within 3 to 5 seconds. If too much time proceeds between the addition of **5** and $NaBH_4$, large chunks of precipitate form that render the Pt^{4+} inaccessible to $NaBH_4$. When this happens, the yield of nanoparticles is low. It should also be noted that rapid addition of the $NaBH_4$ solution is made difficult by the rapid production of hydrogen bubbles. Thus using a large flask with a large opening is crucial. Despite careful addition of **5** and $NaBH_4$, a small amount of precipitate usually does form. Accordingly, adding methanol 10 minutes after the reduction solvates the precipitate and completes the reduction. Adding the methanol sooner than this is detrimental because changing the water:methanol ratio yields smaller nanoparticles.

After removal of methanol via rotary evaporation, the water is lyophilized (freeze dried) by cooling the solution and attaching the flask to a vacuum line. If the solution is above about 5 °C, a foam forms that makes further removal of water difficult. The water does not need to be completely frozen during the evacuation and typically we placed a bath of luke-warm water beneath the flask after about ten minutes to expedite water removal.

The black solid is transferred by spatula to 50 mL centrifuge tubes (Nalgene Oakridge PTFE tubes). Residual nanoparticles are transferred by dissolution in a small volume of methanol. For a synthesis on the scale described above (2.0 g of $PtCl_4$), distributing the solid into four 50 mL centrifuge tubes is necessary to allow for efficient centrifugation. To each of the centrifuge tubes, approximately 4 mL of methanol is added and the tubes are shaken for several minutes to dissolve most of the solid. Ether is added to the fill mark. The tubes are centrifuged at 10,000 rpm for 2 minutes. The faintly colored (light brown) supernatant is decanted. The centrifugation with methanol and ether is repeated three more times.

To remove NaCl, the solid is dissolved in a solution of 3 g of methanol and 97 g of $CHCl_3$. The solution is poured through Whatman filter paper. The remaining solid in the filter is washed four more times with 50 mL of 3 wt.% methanol and 97 wt.% $CHCl_3$. The solvent is rotary evaporated from the nanoparticles. The nanoparticles are centrifuged four more times in methanol/ether as before and one last time in ether. The black solid is broken into a fine powder using a mortar and pestle (*Caution! Dry nanoparticles should always be handled in a fume hood to prevent inhalation.*) Finally,

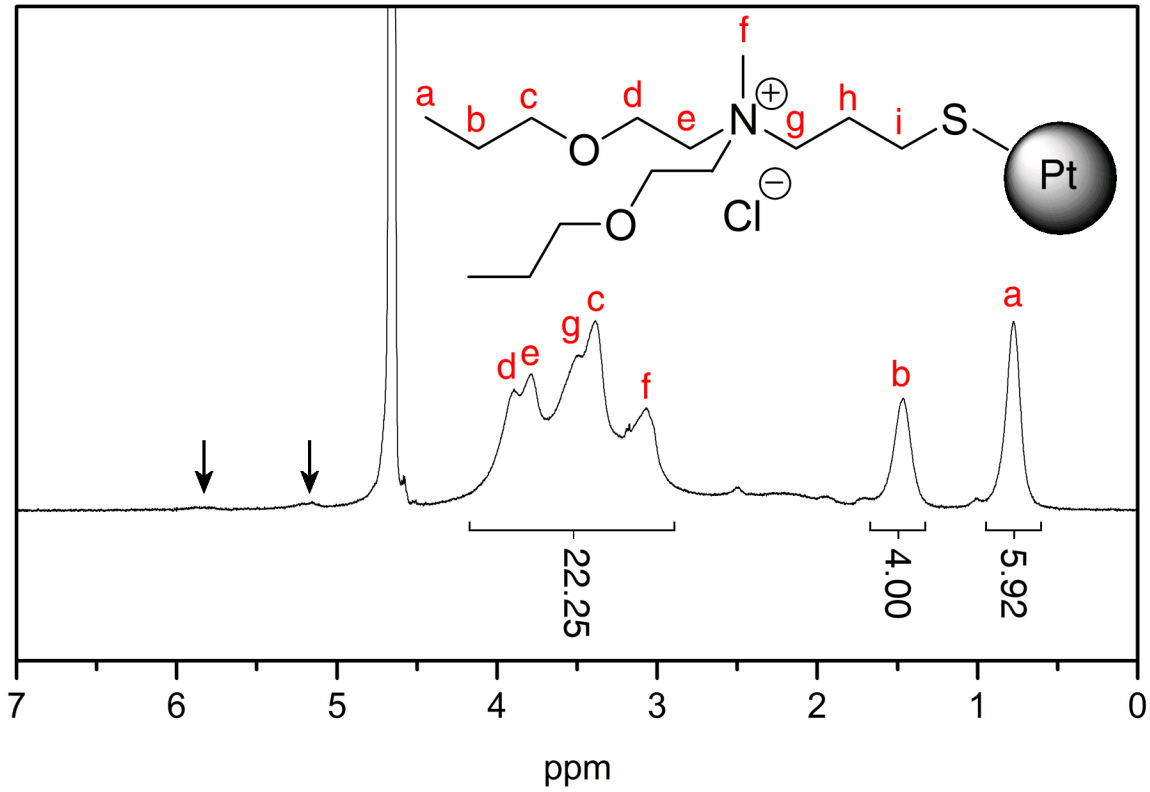

Figure S9. ^{1}H NMR of as-synthesized Pt nanoparticles. During the synthesis, the double bond becomes hydrogenated (arrows show a small amount of unhydrogenated ligand). Peaks **h** and **i** are not observed because of proximity to the platinum surface (*3*). Peak assignments for **c** through **g** are tentative. (D_2O, 300 MHz) δ 3.90 (**d**, 4H), 3.79 (**e**, 4H), 3.49 (**g**, 2H), 3.39 (**c**, 4H), 3.07 (**f**, 3H), 1.46 (**b**, 4H), 0.77 (**a**, 4H).

the powder is transferred to a round bottom flask and evacuated on a vacuum line for about an hour to remove remaining solvent. A ^{1}H NMR spectrum is shown in Figure S9.

The purified, as-synthesized nanoparticles were subjected to an ageing process in boiling water. To a 500 mL flask with stirbar, we added 0.68 g of as-synthesized Pt nanoparticles and 230 g of water. A reflux condenser was attached and the flask was heated in an oil bath held at 115 °C. Five hours after first placing the flask in the pre-

heated oil bath, the flask was removed and allowed to cool naturally to room temperature. Following this, the water was lyophilized and the resulting black solid was centrifuged four times in methanol/ether and once in ether as described above. The solid was pulverized in a mortar and pestle and dried on a vacuum line for several hours. A ^{1}H NMR spectrum is shown in Figure S10. The NMR shows that there are a very small number of impurities (integration of the impurities accounts for 1.8% of the total integrated area in the spectrum) and the fact that these appear as sharp peaks indicate that they are not directly associated with the nanoparticle. Thus NMR suggests that ageing the particles causes minimal changes in the composition of the organic material that is bound to the nanoparticles (although TGA measurements, shown later, demonstrate that there are fewer ligands per particle). Nevertheless, liquid-phase ^{1}H NMR does a poor job of identifying organic material immediately adjacent to the surface (*3*) so we cannot rule out the possibility that there are relatively short organic (or inorganic) species bound to the nanoparticle surface.

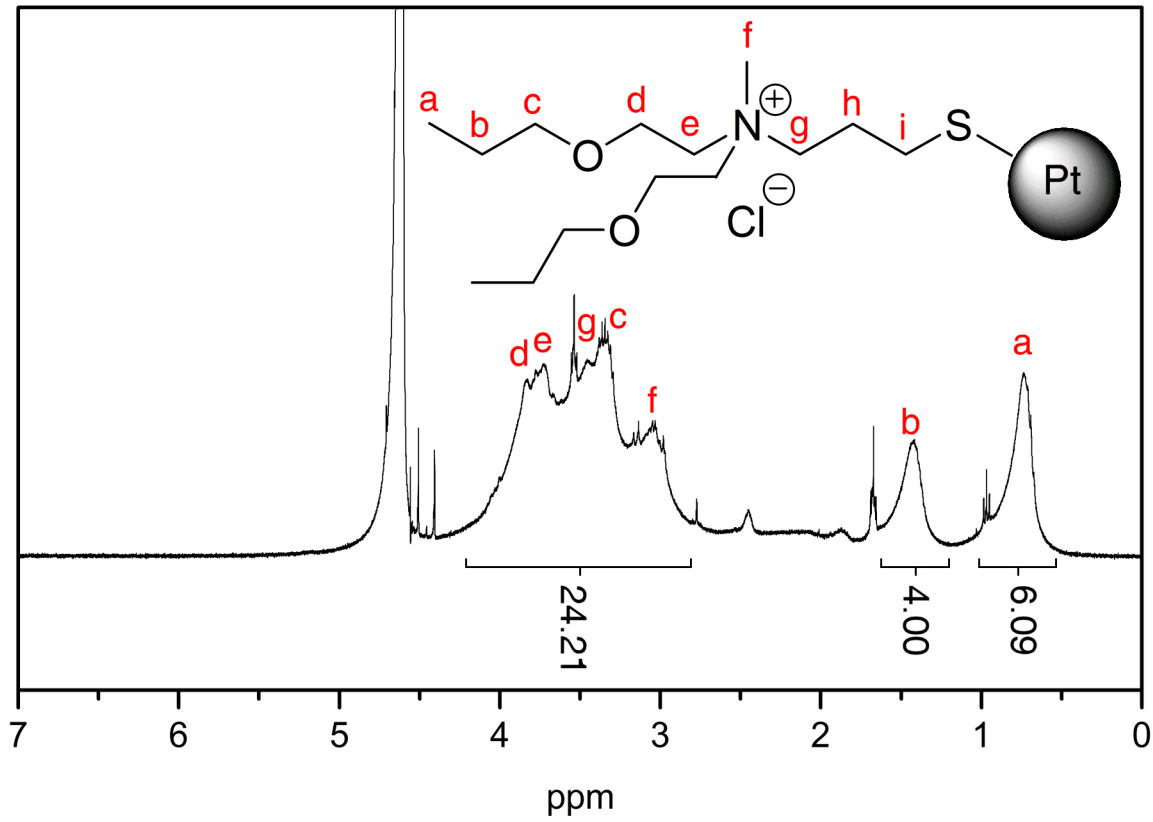

Figure S10. ^{1}H NMR of aged Pt nanoparticles. Peak assignments for **c** through **g** are tentative. (D_2O, 300 MHz) δ 3.87 (**d**, 4H), 3.74 (**e**, 4H), 3.49 (**g**, 2H), 3.38 (**c**, 4H), 3.08 (**f**, 3H), 1.46 (**b**, 4H), 0.78 (**a**, 4H).

TGA

TGA was performed in air and nitrogen on as-synthesized and aged nanoparticles (Figure S11), on as-synthesized and annealed CCM-Pt-6 hybrids (Figure S12), and on the CCM-Pt-6 pyrolized and acid-treated films (Figure S13). We assumed that only platinum metal remains after performing TGA in air. We believe this is a good assumption because the resulting material is reflective and platinum-colored like bulk Pt. From TGA, we conclude that the aging process leads to a loss of ligands from the nanoparticles. Comparison of aged particles heated in air with those heated in nitrogen

show that 18 wt.% of the ligand remains after pyrolysis. Also noteworthy is the fact that most of the mass loss occurs between 150 °C and 250 °C when heating under nitrogen. In contrast, pyrolysis of the PI-*b*-PDMAEMA block copolymer by itself (data not shown) occurs mostly between 320 °C and 420 °C. Thus, two clearly defined mass loss steps are observed in the CCM-Pt-6 nanoparticle-block copolymer hybrids when heated under nitrogen (Figure S12). When heated in air, the mass loss is greater and the difference in mass loss reflects the approximate mass of carbonaceous material that remains in the pyrolized samples. In Figure S12, it is also evident that the annealed hybrids have less organic material than the as-made hybrids. Presumably during the annealing process (2 days at 130 °C under vacuum) the ligands partially decompose and volatilize. Indeed, comparison of the as-made and annealed hybrids show that the differences in mass loss occur primarily at temperatures below 275 °C, which we assign to ligand decomposition (as noted above).

The CCM-Pt-6 platinum-carbon nanocomposite apparently absorbs a significant quantity of water or other volatile species from the atmosphere; these species rapidly evaporate during TGA (Figure S13). There is a small increase in mass at 200 °C which may arise from the partial oxidation of the carbonaceous matrix. TGA suggests that the acid treatment removes nearly all combustible and volatile compounds from the platinum-carbon nanocomposite, consistent with EDS (Figure 4 C). The absence of a significant mass loss at temperatures below 150 °C (as occurs with the platinum-carbon nanocomposite) suggests that the carbonaceous matrix is where the adsorbed water and other volatile species primarily reside.

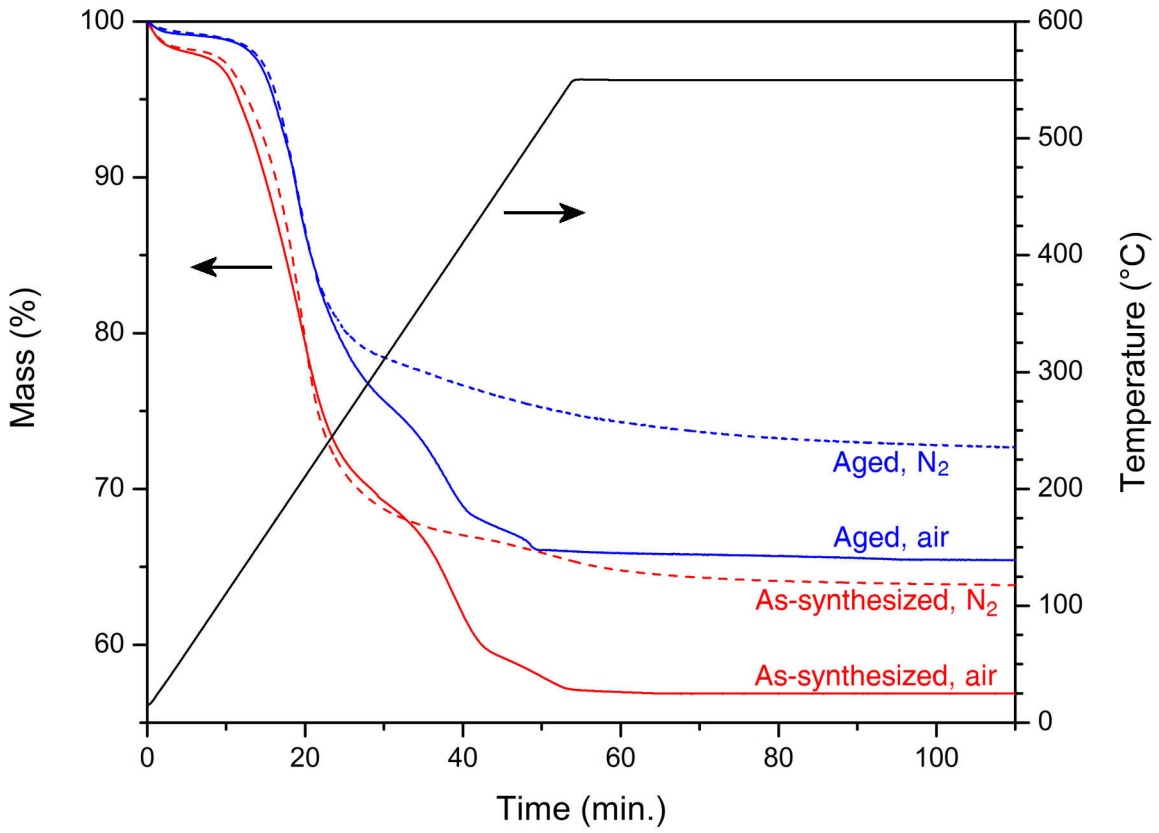

Figure S11. TGA traces of platinum nanoparticles. For all runs, the nanoparticles were heated at 10 °C/min. to 550 °C under flowing N_2 or air and held at 550 °C for one hour (black line).

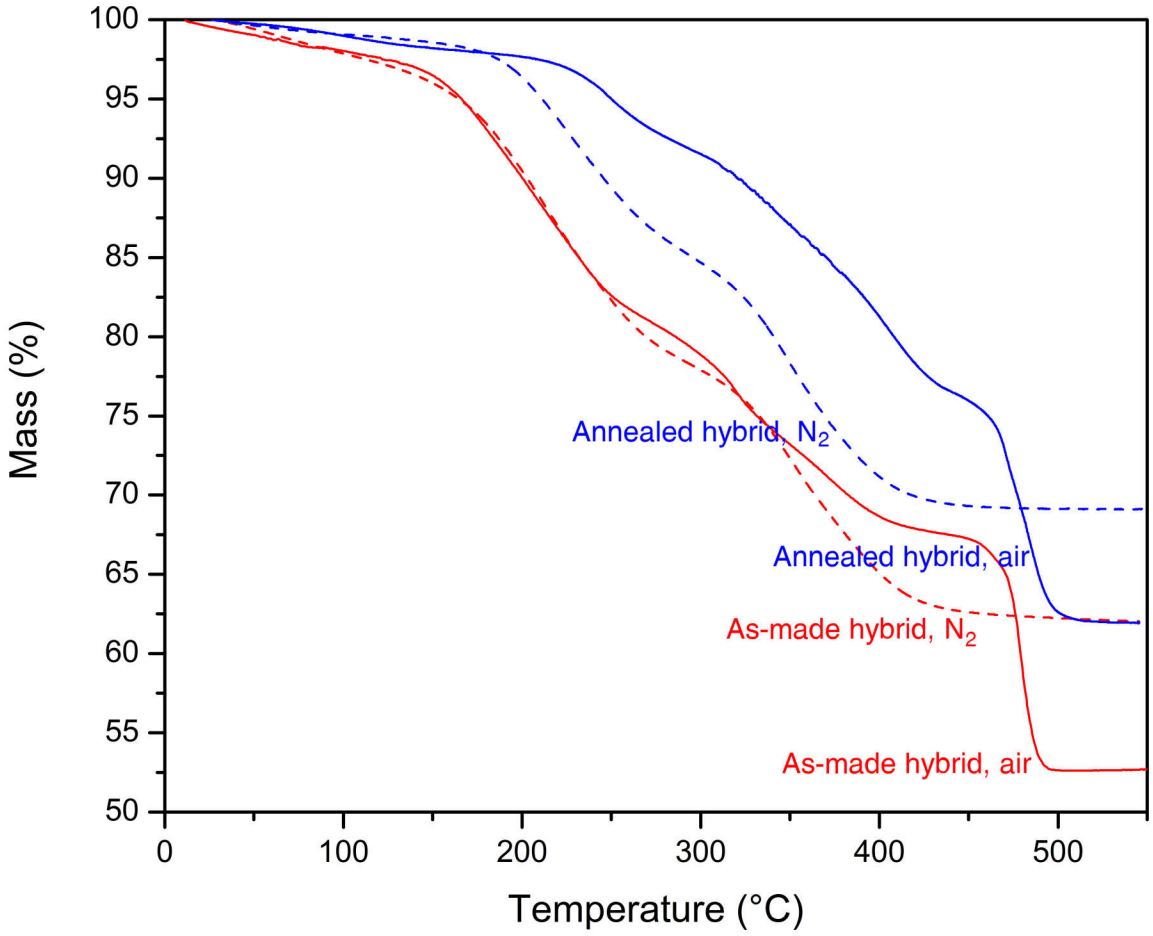

Figure S12. TGA of CCM-Pt-6 hybrids, before and after annealing. For all runs, the hybrids were heated at 10 °C/min. to 550 °C.

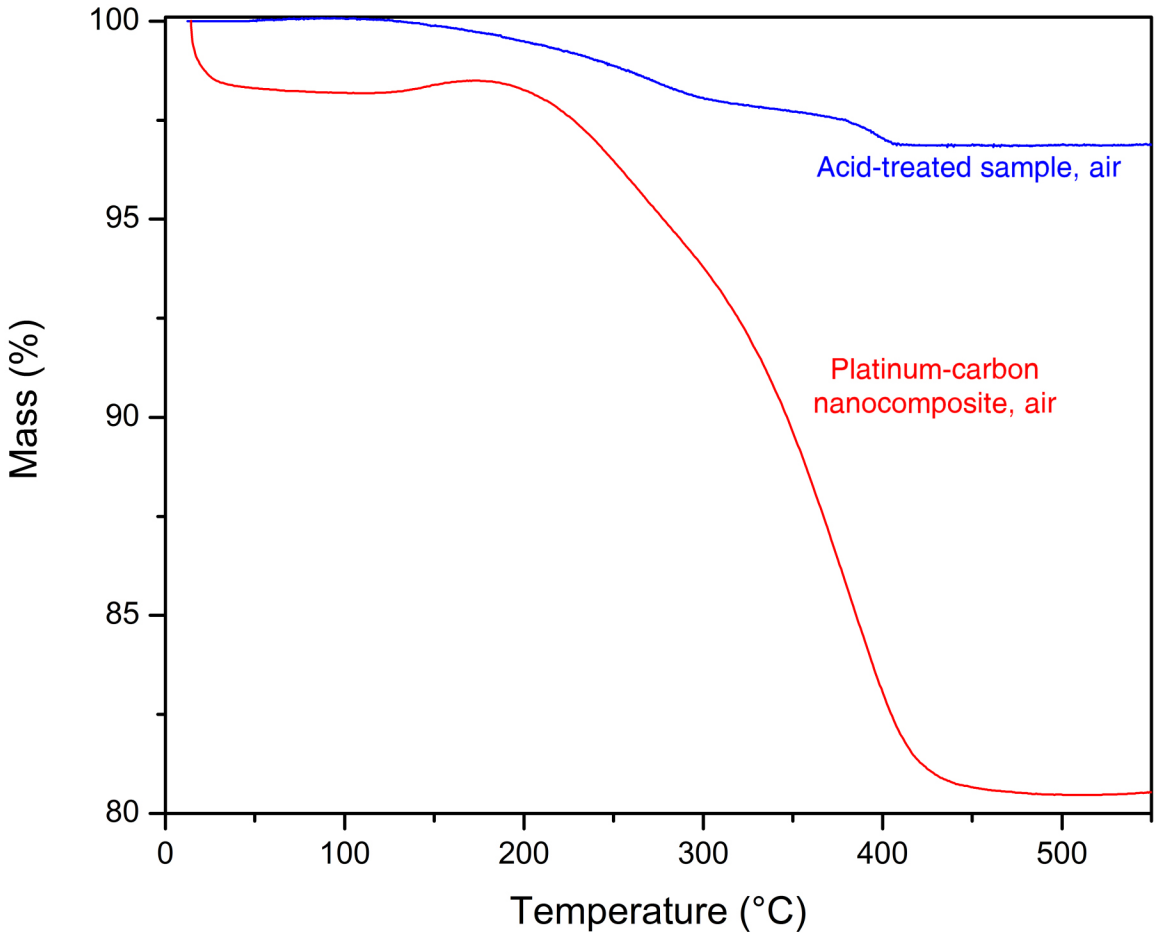

Figure S13. TGA of CCM-Pt-6 platinum-carbon nanocomposite and acid-treated sample. Both samples were heated in air at 10 °C/min. to 550 °C.

Calculations

To calculate the platinum and organic volume fraction in the nanoparticles, we assumed that the platinum nanoparticles were spherical and that the platinum core had the density of bulk platinum (21.09 g/cm^3). We assumed the mass loss observed when performing TGA in air corresponded to the total mass of ligand and that only platinum remained after combustion. We also assumed that the composition of the ligand on the nanoparticle was the same as ligand **5** prior to the nanoparticle synthesis (see Figure S7),

which consisted of a mixture of chloride salt (313.9 g/mol, ~60%) and bromide salt (358.4 g/mol, ~40%) and thus has an averaged molecular weight of 331.7 g/mol.

A spherical platinum nanoparticle (metal core diameter of 1.83 nm) has a volume of 3.21 nm^3. This volume of metal weighs 67.7 zg (z = zepto = 10^{-21}) and contains 209 platinum atoms. The as-synthesized platinum nanoparticles had a mass loss in TGA of 43.1%. From this we calculate that the mass of ligands attached to each nanoparticle is 51.3 zg, which suggests that approximately 93 ligands are attached to each nanoparticle, on average.

$$\text{mass of Pt} = \frac{4}{3}\cdot\pi\cdot\left(\frac{1.83\,\text{nm}}{2}\right)^3\cdot\left(\frac{1\,\text{cm}^3}{10^{21}\,\text{nm}^3}\right)\cdot\frac{21.09\,\text{g}}{\text{cm}^3} = 67.7\cdot10^{-21}\,\text{g} = 67.7\,\text{zg} \qquad [1]$$

$$\#\,\text{of Pt atoms} = \frac{67.7\cdot10^{-21}\,\text{g}}{195\,\text{g/mol}}\cdot\frac{6.022\cdot10^{23}\,\text{atoms}}{\text{mol}} = 209\,\text{atoms} \qquad [2]$$

$$\#\,\text{of ligands per particle} = \frac{\left(\frac{67.7\cdot10^{-21}\,\text{g}}{1-0.431}\right)-67.7\cdot10^{-21}\,\text{g}}{331.7\,\text{g/mol}}\cdot\frac{6.022\cdot10^{23}\,\text{ligands}}{\text{mol}} = 93\,\text{ligands} \qquad [3]$$

A similar calculation for the aged nanoparticles shows that there are 65 ligands per nanoparticle.

The calculation of platinum or ligand volume fraction in the nanoparticles can be performed in several ways. Perhaps the simplest method depends on finding the molar volume of the ligand, which can be done via bulk density measurements or computational approaches. We used both approaches and found both gave very similar results. Optimizing the molecular structure using a variety of packages (MM2, Mopac) and

calculating the atomic volume yielded approximately 0.440 nm^3 for the bromide salt of **5** and 0.430 nm^3 for the chloride salt of **5**. Conversion to a bulk density yields 1.3 g/cm^3, which is identical to our measured bulk density. Using this density, the TGA data can be used to calculate platinum and ligand volume fractions. Thus we calculate that the platinum volume fraction is 7.5% and 10.4% in the as-synthesized and aged particles, respectively.

$$\text{molar volume} = \left(\frac{0.440\ \text{nm}^3}{\text{ligand}} \cdot 0.4 + \frac{0.430\ \text{nm}^3}{\text{ligand}} \cdot 0.6 \right) \cdot \frac{\text{cm}^3}{10^{21}\ \text{nm}^3} \cdot \frac{6.022 \cdot 10^{23}\ \text{ligands}}{\text{mol}} = \frac{261\ \text{cm}^3}{\text{mol}} \quad [4]$$

$$\text{ligand density} = \frac{331.7\ \text{g/mol}}{261\ \text{cm}^3/\text{mol}} = 1.3\ \text{g/cm}^3 \quad [5]$$

$$\text{platinum volume fraction} = \frac{\frac{56.9\ \text{wt.\%}}{21.09\ \text{g/cm}^3}}{\frac{43.1\ \text{wt.\%}}{1.3\ \text{g/cm}^3} + \frac{56.9\ \text{wt.\%}}{21.09\ \text{g/cm}^3}} = 7.5\ \text{vol.\%} \quad [6]$$

To calculate the volume fraction of the hydrophilic and hydrophobic components in the CCM-Pt-4 and CCM-Pt-6 hybrids, we converted the weights of the PI, PDMAEMA, and nanoparticles into volume fractions. We assumed that the PI and PDMAEMA in the hybrid had densities similar to their bulk values, i.e., 0.91 g/cm^3 and 1.15 g/cm^3, respectively. Table S1 outlines the quantities and volumes for the CCM-Pt-6 inverse hexagonal hybrid and Table S2 displays those of the CCM-Pt-4 lamellar hybrid. Lamellar hybrids were made from both PI-*b*-PDMAEMA block copolymers described in the polymer synthesis section, above. It is certainly noteworthy that hybrids self-assemble into an ordered structure during annealing and that the annealing process also

leads to loss of ligand. This decreases the hydrophilic volume fraction and is accounted for in the second set of columns. To determine the mass loss during annealing (15%), we assumed that both samples (as-synthesized and annealed) consisted solely of platinum following heat-treatment in air (Figure S11). Thus we were able to equate the masses of the two samples at the end of the TGA run and back-calculate their relative starting masses (prior to the TGA analysis). The as-synthesized hybrid retained 52.6% of its original mass and the annealed hybrid retained 62.0%. Compared to the starting mass of the annealed hybrid (100%), the as-synthesized hybrid had a mass of 100% · 62.0% / 52.6% = 118%. With respect to the as-synthesized hybrid, the annealed hybrid lost 100% - (100% / 118%) = 15% during annealing.

Table S1. Volume fraction calculations for CCM-Pt-6. The mass of PI-*b*-PDMAEMA is 27.6 mg, of which 33 wt.% is PDMAEMA. The mass of the aged platinum nanoparticles is 97.5 mg, of which 65 wt.% is Pt.

	As-made				Annealed			
	Density (g/mL)	Mass (mg)	Volume (mL)	Volume %	Density (g/mL)	Mass (mg)	Volume (mL)	Volume %
PI	0.91	18.4	20.2	35.5	0.91	18.4	20.2	47.6
PDMAEMA	1.15	9.1	7.9	13.8	1.15	9.1	7.9	18.6
Pt	21.09	63.8	3.0	5.3	21.09	63.8	3.0	7.1
Ligand	1.3	33.7	25.9	45.4	1.3	14.7	11.3	26.7
Hydrophilic	2.89	106.6	36.8	64.5	3.94	87.6	22.3	52.4

Table S2. Volume fraction calculations for CCM-Pt-4. The mass of PI-*b*-PDMAEMA is 33.7 mg, of which 33 wt.% is PDMAEMA. The mass of the aged platinum nanoparticles is 73.2 mg, of which 65 wt.% is Pt.

	As-made				Annealed			
	Density (g/mL)	Mass (mg)	Volume (mL)	Volume %	Density (g/mL)	Mass (mg)	Volume (mL)	Volume %
PI	0.91	22.6	24.8	44.1	0.91	22.6	24.8	56.7
PDMAEMA	1.15	11.1	9.7	17.2	1.15	11.1	9.7	22.1
Pt	21.09	47.9	2.3	4.0	21.09	47.9	2.3	5.2
Ligand	1.3	25.3	19.5	34.6	1.3	9.1	7.0	16.0
Hydrophilic	2.69	84.3	31.4	55.9	3.60	68.1	18.9	43.3

References

1. S. Creutz, P. Teyssie, R. Jerome, *Macromolecules* **30**, 6-9 (1997).
2. S. Renker, *Dissertation*, Max Planck Institute for Polymer Research (2003).
3. R. H. Terrill *et al.*, *J. Am. Chem. Soc.* **117**, 12537-12548 (1995).